Aging-dependent microglial heterogeneity worsens outcomes in models of traumatic brain injury

Zhichao Lu[1,4,10], Yi Shuai[7,10], Chenxing Wang[1,4,10], Zongheng Liu[8,10], Ziheng Wang[5,6], Qianqian Liu[1,4], Rui Jiang[1,4], Jue Zhu[1,4], Yongqi Zhu[1,4], Weiquan Liao[1,4], Xingjia Zhu[1,4], Jingwei Zhao[9], Kaibin Shi[2,3*], Wei Shi[1,4*], Peipei Gong[1,4*]

1 Department of Neurosurgery, Research Center of Clinical Medicine, Affiliated Hospital of Nantong University, Medical School of Nantong University, Nantong, Jiangsu, China.

2 Department of Neurology, China National Clinical Research Center for Neurological Diseases, Beijing Tiantan Hospital, Capital Medical University, Beijing, China.

3 Chinese Institute for Immunology, Chinese Institutes for Medical Research, Beijing, China.

4 Neuro-Microscopy and Minimally Invasive Translational Medicine Innovation Center, Affiliated Hospital of Nantong University, Nantong, Jiangsu, China.

5 MOE Frontier Science Centre for Precision Oncology, University of Macau, Macau SAR, China.

6 The School of Public Health and Preventive Medicine, Monash University, Melbourne, Victoria, Australia.

7 Faculty of Medicine, The Chinese University of Hong Kong, Shatin, Hong Kong Special Administrative Region, China.

8 Department of Neurosurgery, Zhejiang Provincial Hospital of Chinese Medicine, The First Affiliated Hospital of Zhejiang Chinese Medical University, Hangzhou, Zhejiang, China.

9 Department of General Surgery, Xinhua Hospital, Affiliated to Shanghai Jiao Tong University School of Medicine, Shanghai, 200092, China.

10 These authors contributed equally.

*Corresponding Authors

Peipei Gong, Address: Department of Neurosurgery, Research Center of Clinical Medicine, Affiliated Hospital of Nantong University, Medical School of Nantong University, Nantong, Jiangsu, China., E-mail: ntgpp@ntu.edu.cn.

Wei Shi, Address: Department of Neurosurgery, Research Center of Clinical Medicine, Affiliated Hospital of Nantong University, Medical School of Nantong University, Nantong, Jiangsu, China., E-mail: fysw@ntu.edu.cn.

Kaibin Shi, Address: Department of Neurology, China National Clinical Research Center for Neurological Diseases, Beijing Tiantan Hospital, Capital Medical University, Beijing, China., E-mail: kshi@cimrbj.ac.cn.

Conflict of interest

The authors have declared that no conflict of interest exists.

Abstract

Traumatic brain injury (TBI) disproportionately affects the elderly, yet the underlying mechanisms remain unclear. Here, we demonstrate that aged TBI brains predominantly harbor pro-inflammatory NLRP3^{+} microglia, in stark contrast to the neuroprotective Lysozyme^{+} microglia prevalent in young TBI brains. This age-dependent microglial dichotomy correlates with elevated mortality and impaired recovery in aged TBI mice. By leveraging an integrative multi-omics approach combined with metabolomics and epigenome analysis, we identify a previously unrecognized link between enhanced glycolysis and pro-inflammatory chromatin landscape in NLRP3^{+} microglia. Further investigation identifies ELF1 as a key transcription factor driving NLRP3^{+} microglia formation. Importantly, ablation of ELF1 reverses age-associated microglial dysfunction and improves TBI outcomes. Finally, we discover that Imeglimin, a clinically approved antihyperglycemic agent capable of crossing the blood brain barrier, inhibits ELF1 and reverses microglial phenotype, reducing acute mortality rate and leading to improved functional recovery of aged TBI mice. Our work elucidates the mechanistic basis of age-dependent TBI outcomes, reveals the crosstalk between metabolic rewiring and epigenetic regulation in microglial aging, and identifies ELF1 as a promising therapeutic target for improving TBI outcome.

Keywords: Microglia, Traumatic brain injury, Neuroinflammation, Single-cell sequencing, Multi-omics

Introduction

Traumatic brain injury (TBI) is a leading cause of death and long-term disability globally (1, 2), but lack of effective pharmacologic treatments (3). Epidemiologically, the frequency of hospital admissions is highest in patients over 65 years old, with a mortality rate more than double that of younger populations. Additionally, aged survivors often experience substantial impairments in quality of life (4, 5). Aging has profound effects on the immune responses, but how these age-related changes worsen the prognosis of TBI remains unclear (6, 7).

Microglia are resident immune cells in the central nervous system (CNS) and play a key role in maintaining CNS homeostasis and mediating responses to injury (8, 9). In aging and neurodegenerative conditions, microglia lose their balanced functional profile, exhibiting impairments such as enhanced pro-inflammatory cytokine production, increased reactive oxygen species (ROS) release, and compromised phagocytosis marked by lysosomal deposition (10-12). Recent single-cell transcriptomics studies have revealed remarkable heterogeneity among microglia, including "disease-associated microglia" (DAM), which is a dysfunctional microglia phenotype (13-15). While these studies highlight microglial plasticity, critical gaps remain in our understanding of how aging reshapes the composition and functional properties of microglial subpopulations after TBI. Specifically, it remains unclear whether age-driven shifts in microglial subsets contribute to the worse outcomes observed in aged TBI patients, and if so, what molecular and cellular clues underlying these effects.

Emerging evidence suggests that metabolic rewiring and epigenetic regulation are key drivers of microglial functional polarization (16, 17). For instance, pro-inflammatory microglia often rely on glycolysis for energy, whereas anti-inflammatory or homeostatic microglia favor

oxidative phosphorylation (OXPHOS) and the tricarboxylic acid (TCA) cycle (17). Aging has been shown to disrupt microglial metabolism, but how these metabolic changes intersect with transcriptional and epigenetic alterations to shape microglial heterogeneity post-TBI is not well defined. Additionally, transcription factors (TFs) that orchestrate age-specific microglial phenotypes remain largely uncharacterized, presenting a critical gap in identifying potential therapeutic targets.

Given the unmet need to explain age-dependent TBI outcomes and the critical role of microglia in neuroinflammation, we hypothesized that aging induces selective expansion of pro-inflammatory microglial subsets and impairment of neuroprotective subsets, driven by coordinated metabolic reprogramming and epigenetic remodeling. To test this hypothesis, we examined the injured cerebral hemisphere in aged and young mice with TBI by single-cell sequencing to investigate the effects of aging on the brain immune microenvironment after TBI. After TBI, the brains of aged patients and mice have a stronger inflammatory response, as evidenced by a massive infiltration of immune cells characterized by a strong microglia response. In this study, we identified a population of $NLRP3^+$ microglia that worsened the prognosis of aged patients and mice after TBI. The results of untargeted metabolomics and ATAC-seq identified impaired energy metabolism in $NLRP3^+$ microglia with higher chromatin accessibility to pro-inflammatory markers. Using the SCENIC algorithm and Motfit enrichment, combining with the CRISPR/ Cas9 system, we identified a group of TFs (*ELF1*, *NFKB2*, *RELA*, *FLI1*, *NFKB1*, *JUN*, *JUNB*, and *FOSB*) that may collectively regulate $NLRP3^+$ microglia formation, with ELF1 playing the most prominent role. Imeglimin, a newly marketed antihyperglycemic agent (18), blocks the action of ELF1 and reduces the population of $NLRP3^+$

microglia after TBI leading to an improved prognosis in mice, especially aged mice, after TBI.

Results

1. Microglia responses are more severe in aged TBI patients and mice

Aged TBI patients often show poorer recovery and higher mortality than younger individuals, which may potentially mediate by exaggerated neuroinflammation in the aged. To comprehensively characterize how aging affects brain inflammatory response after TBI, we used a droplet-based single-cell RNA sequencing (scRNA-seq) technique to isolate cells from the injured hemisphere of aged and young mice at 72-h after TBI modeling, which was designed to observe transcriptome alterations during the acute phase (Figure 1A). We performed unsupervised clustering and cell type annotation based on classical gene markers. As shown in the Uniform Manifold Approximation and Projection (UMAP) plot, 12 distinct cell types were identified, including oligodendrocytes (19721), microglia (61707), macrophages (5688), fibroblasts (3239), astrocytes (2735), epithelial cells (8267), endothelial cells (27796), neurons (1824), T cells (2661), B cells (1183), granulocytes (2384), and monocytes (2139) (Figure 1, B and D, and Supplemental Table 1). Consistent with previous findings, we also identified the presence of circulating immune cells such as macrophages, monocytes, neutrophils and T/B cells in the brain after TBI (19, 20).

In aged mice, significant microglia proliferation was observed following TBI, whereas this phenomenon was not prominent in young mice (Figure 1C, and Supplemental Figure 1, A and B). Orthogonal validation via flow cytometry confirmed the findings from scRNA-seq. Specifically, TBI led to a significant increase in microglial abundance, with aged microglia showing a more pronounced expansion compared to their young counterparts (Supplemental Figure 1, C and D).

TBI induced extensive differential gene regulation, with microglia populations showing the most pronounced changes (Figure 1E). Notably, aged microglia exhibited the highest number of differentially expressed genes (DEGs) compared to their young counterparts after TBI, highlighting distinct age-specific transcriptional remodeling in microglia post-injury (Figure 1F). Signature of aged microglia after TBI was associated with a pro-inflammatory phenotype, including genes involved in inflammatory responses (e.g. *Tnf*, *Nod2*, *Il6* and *Tlr4*), NLRP3 inflammasome complex related genes (e.g. *Nlrp3*, *Il1b* and *Casp1*), genes involved in cellular chemotaxis and adhesion (*Fn1*, *Ccl5*, *Icam1* and *Itga7*) and myeloid cell activation-related genes (*Cd68*, *Nos2* and *H2-Aa*), however genes related to microglia homeostasis (*Havcr2*, *Mef2c, Il4* and *Tgf1*) were down-regulated in microglia from aged TBI mice (Figure 1G).

To translate these preclinical findings to a clinical context, we obtained injured brain tissue samples from 13 young TBI and 22 aged TBI patients who underwent surgery and examined the proportion of microglia. Consistent with the insights obtained from murine models, aged TBI patients exhibited a more robust microglial response compared to young patients (Supplemental Figure 1, E and F). Quantitative reverse transcription polymerase chain reaction (qRT-PCR) of patients' microglia revealed the distinct age-specific cytokine expression profiles, pro-inflammatory cytokines *IL1B*, *IL6* and *TNF* were significantly up-regulated in microglia from aged patients; whereas the transcripts of anti-inflammatory cytokines *IL4*, *IL10* and *TGFB1* were up-regulated in microglia from young patients (Supplemental Figure 1G).

2. NLPR3^{+} microglia orchestrate detrimental outcomes in aged TBI

To decipher how aging affects the transcriptional profile of microglia after TBI, we clustered microglia from different samples and observed substantial heterogeneity among microglia after TBI. The UMAP plot shows five different states consisting of *Nlrp3*$^+$ (*Nlrp3*$^+$*Il1b*$^+$*Casp1*$^+$), *Lyz2*$^+$ (*Lyz2*$^+$*Cst7*$^+$*Spp1*$^+$), *Ccl5*$^+$ (*Ccl5*$^+$*Cxcl10*$^+$), *Nav2*$^+$ (*Nav2*$^+$*Runx1*$^+$), and *H2-Eb1*$^+$ (*H2-Eb1*$^+$*H2-Ab1*$^+$) microglia after TBI (Figure 2, A-C). For instance, *H2-Eb1*$^+$ microglia exhibit high expression of major histocompatibility complex (MHC)-II molecules, representing a population of microglia that may have antigen-presenting capacity. We identified clusters that may represent features of the inflammatory response (*Nlrp3*$^+$) and specific chemotaxis (*Ccl5*$^+$). Some subsets of our data show partial concordance with published states, characteristic genes of *Lyz2*$^+$ microglia such as *Cst7* and *Spp1* are widely identified in stage2 DAM (15, 21), and the sensitivity of *Lyz2*$^+$ microglia to IL-4 suggests its important role in limiting neuroinflammation (Figure 2D). In summary, our microglial atlas not only captures known microglia subpopulation features, but also reveals potentially uncharacterized microglia subpopulations.

Nlrp3$^+$ cluster representing neuroinflammatory responses being upregulated in aged microglia after TBI, while *Lyz2*$^+$ cluster representing tissue repair as well as myeloid homeostasis was shown enhanced enrichment in young microglia (Figure 2B). To test the representativeness of the markers for each microglia cluster suggested by scRNA-seq, we used the cluster 0-specific marker NLRP3 and the cluster 1-specific marker Lysozyme (the protein encoded by the *Lyz2* gene) to label different clusters of microglia. The proportion of NLRP3$^+$ microglia infiltrating the injured area was higher in aged TBI mice, whereas the opposite was true for Lysozyme$^+$ microglia (Figure 2, E and F, and Supplemental Figure 2). To extend this

finding to a broader spectrum of brain injury states, we validated it in mice models of repetitive mild TBI (rmTBI). In rmTBI mice, our findings still hold, with aged mice characterized by enhanced NLRP3^{+} microglia responses whereas young microglia exhibit increased Lysozyme^{+} phenotype after brain injury (Supplemental Figure 3, A-D). Flow cytometry and representative immunofluorescence results of different ages TBI patients corroborated the insights generated from TBI mice that aged microglia responses after TBI were dominated by NLRP3^{+} cluster, whereas young microglia responses were dominated by Lysozyme^{+} cluster (Figure 2, G and H, Supplemental Figure 4, and Supplemental Figure 5).

To investigate the effect of different microglia subpopulations on the prognosis of TBI patients, we used AAV-*Cx3cr1-Cre* virus to knockout microglial *Nlrp3* in *Nlrp3*$^{fl/fl}$ mice after TBI. Through Ai9 reporter mice, we confirmed the specificity of this microglia-targeting strategy (Supplemental Figure 6, A-E). Flow cytometry confirmed the specific deletion of NLRP3 in microglia (Supplemental Figure 7, A and B). After knockout *Nlrp3* in microglia, TBI mice exhibited lower mortality, and better neurological recovery (lower mNSS scores, and prolonged latency to fall from the rotarod test) (Figure 2, I and K-L). Further, we explored the efficacy of MCC950, a selective inhibitor of NLRP3. MCC950 administration reduced mortality and NLRP3^{+} microglia responses in the acute-phase aged TBI mice (Supplemental Figure 8, A-D). Suppression of neuroinflammation after MCC950 treatment significantly improved neurological recovery in aged TBI mice (Supplemental Figure 8E). Interestingly, we also found that MCC950 prevented the brain infiltration of circulating lymphocytes after TBI by suppressing the transcription of lymphocyte chemotactic factor in microglia (Supplemental Figure 8, F-I).

In contrast, after knockout microglial *Lyz2*, both aged and young TBI mice exhibited higher mortality and worsen neurologic prognosis (higher mNSS scores and shorter latency to fall from the rotarod tests) (Figure 2, J and M-N, and Supplemental Figure 7C). Taken together, these findings suggest that the age-specific signature of enhanced NLRP3$^+$ microglial responses coupled with impaired Lysozyme$^+$ microglial function may contribute to the poorer prognosis of aged mice following TBI.

3. Metabolic reprogramming underlies pro-inflammatory phenotype of NLRP3$^+$ microglia

To unravel the mechanisms underlying the enhanced pro-inflammatory response of aged microglia, we performed gene set variation analysis (GSVA) comparing NLRP3$^+$ microglia and Lysozyme$^+$ microglia. GSVA indicated that NLRP3$^+$ microglia upregulate inflammation-related signaling pathways (Figure 3A). Notably, NLRP3$^+$ microglia may increase their dependence on glycolysis, while the energy metabolism of young microglia may be dependent on the tricarboxylic acid (TCA) cycle and oxidative phosphorylation (OXPHOS). This observation was validated by analyzing the expression of genes associated with these target metabolic pathways by AddModuleScore (Figure 3, B and C). Subsequently, we detected real-time changes in extracellular acidification rate (ECAR) and oxygen consumption rate (OCR) in NLRP3$^+$ microglia and Lysozyme$^+$ microglia by Seahorse. We observed aging-induced increases in ECAR and decreases in OCR, representing the enhancement of cellular glycolysis along with the weakening of TCA, which was consistent with our findings in scRNA-seq (Figure 3, D and E).

Microglial function is closely related to the metabolic state (16). To further characterize

age-related metabolic differences in microglia post-TBI, we purified microglia from aged and young TBI mice via fluorescence-activated cell sorting (FACS) and performed untargeted metabolomics analysis. Aging drove distinct metabolic remodeling in microglia, with $NLRP3^+$ microglia separating from $Lysozyme^+$ microglia along principal component 1, which accounted for 88.6% of the variance (Figure 3F). We observed that NADH and $FADH_2$ equivalents providing for ATP generation by the electron transport chain (ETC) were significantly decreased in $NLRP3^+$ microglia (Figure 3G). For this reason, we explored the metabolites associated with TCA activity in microglia. Notably, we detected a decrease in most TCA intermediates in $NLRP3^+$ microglia, including acetyl coenzyme A (Acetyl-CoA), α-ketoglutarate (α-KG), citrate, and malate (MA) (Figure 3H).

To directly validate the glycolytic flux in microglial subsets, we have performed U-$^{13}C_6$-glucose metabolic tracing experiments and analyzed the isotope labeling patterns of glycolytic intermediates. After incubating sorted microglia with U-$^{13}C_6$-glucose for 60 minutes, $NLRP3^+$ microglia from aged TBI mice show significantly higher ^{13}C-labeling efficiency in glyceraldehyde-3-phosphate (G3P), pyruvate, and lactate compared to $Lysozyme^+$ microglia from young TBI mice (Figure 3I). Collectively, these data suggested that metabolic reprogramming in aging-associated $NLRP3^+$ microglia strongly favors glycolytic dependence.

Previous studies have suggested that metabolic reprogramming of microglia may be associated with altered chromatin accessibility (17, 22). We hypothesized the glycolytic preference of $NLRP3^+$ microglia drive the acquisition of pro-inflammatory chromatin features. To test this, we performed ATAC-seq on $NLRP3^+$ microglia versus $Lysozyme^+$ microglia to reveal the link between metabolic reprogramming and the inflammatory chromatin landscape,

and observed increased chromatin accessibility in NLRP3$^+$ microglia (Figure 3J). Functional enrichment analysis revealed that regions of increased accessibility in the chromatin of NLRP3$^+$ microglia were associated with upregulation of inflammatory responses and inflammation-related signaling pathways (Figure 3K). Importantly, compared to Lysozyme$^+$ microglia, NLRP3$^+$ microglia acquired specific peaks in genes associated with cellular senescence *(Cdkn1a*, *Cdkn2a*), and NLRP3 inflammasome complex (*Nlrp3*, *Casp1*, *Il1b* and *Il18*) (Figure 3L). qRT-PCR further confirmed that NLRP3$^+$ microglia enhanced transcription of senescence-associated secretory phenotype (SASP) markers, including *Cdkn1a*, *Cdkn2a*, *Il1b*, and *Il18* (Supplemental Figure 9A). Overall, our data connects energy metabolism rewiring with altered chromatin accessibility, explaining how aging upregulates the proportion of NLRP3$^+$ microglia after TBI.

4. ELF1 governs the transcriptional features of age-associated NLRP3$^+$ microglia formation

We found that aging-induced impairment of energy metabolism may regulate the inflammatory state of microglia across different age groups by modulating chromatin accessibility. We next sought to identify the intracellular regulators that drive the generation of NLRP3$^+$ microglia, and employed the SCENIC algorithm to dissect the key molecular mechanisms. We found a wide range of inflammatory response-associated transcriptional regulators (TFs) were involved in the development of NLRP3$^+$ microglia. Specifically, genes related to the NF-κB signaling pathway (*Rela*, *Relb*), MAPK signaling pathway (*Fos*, *Jun*), and JAK-STAT signaling pathway (*Stat1*, *Stat3*) were found to be implicated in the formation of NLRP3$^+$ microglia (Figure 4A).

To further characterize NLRP3$^+$ microglia, we validated 29 human homologs of SCENIC-

identified differentially expressed TFs in mouse and human NLRP3$^+$ microglia. 12 TFs (*ELF1*, *NFKB2*, *REL*, *CEBPB*, *RELA*, *FLI1*, *NFKB1*, *STAT3*, *JUN*, *JUNB*, *FOSB*, and *FOS*) were concordantly upregulated in both species, emerging as potential regulators of NLRP3$^+$ microglial formation (Figure 4, B and C). Feature plots confirmed these TFs were barely expressed in Lysozyme$^+$ microglia (Figure 4D). Next, we performed motif enrichment of these selected TFs in ATAC-seq. The results showed that these TFs, which are known to play a key role in mediating the inflammatory cascade response, were enriched in NLRP3$^+$ microglia (Figure 4E).

To identify the key TFs which mainly drive human NLRP3$^+$ microglia formation, we infected a preconstructed Cas9-GFP human microglia cell line (HMC3) with sgRNAs targeting each TF. These cells were mixed with normal HMC3 cells and co-cultured with needle scratch-injured SH-SY5Y neurons (Figure 5A). We quantified the live GFP$^+$/GFP$^-$ microglia ratio and verified genome editing efficiency using *ITGAM*-specific sequences (Figure 5, B and C). We identified 8 TFs (*ELF1*, *NFKB2*, *RELA*, *FLI1*, *NFKB1*, *JUN*, *JUNB*, and *FOSB*) that significantly promote NLRP3$^+$ microglia formation, *ELF1* ablation exhibited the strongest inhibitory effects on NLRP3$^+$ microglia generation and IL-1β secretion (Figure 5, D-F, and Supplemental Figure 11, A and B). Notably, ablation of *ELF1* in microglia had little effect on the microglial viability (Figure 5, G and H). In Cas9$^+$ HMC3 monocultures, three distinct *ELF1*-targeting sgRNAs reduced NLRP3$^+$ microglia formation, ruling out off-target effects (Supplemental Figure 10, A and B).

To clarify the specific role of ELF1 in NLRP3$^+$ microglia formation, we established a THP-1-Cas9-GFP cell line and knock out *ELF1*. While *ELF1* ablation attenuated TBI-induced

IL-1β secretion in THP-1 cells, the effect was weaker than in HMC3 cell line. Quantitative comparison further confirms that ELF1 plays a far more prominent role in regulating inflammation in microglia than peripheral myeloid cells (Supplemental Figure 11, C-H).

5. Ablation of *Elf1* reversed aging related microglia dysfunction and improves the outcome of TBI mice

To further investigate ELF1's in vivo regulation of microglial inflammatory responses, we crossed $Elf1^{fl/fl}$ mice with $Cx3cr1^{creERT2}$ mice (Cre-only) and constructed $Elf1^{fl/fl}$; $Cx3xr1^{CreERT2}$ mice (cKO) to selectively ablate *Elf1* expression in $CX3CR1^{+}$ cells. To rule out a potential effect of *Elf1* deletion on brain development, *Elf1* was deleted only after tamoxifen administration. Specifically, tamoxifen induced ablation of *Elf1* in cells expressing *Cx3cr1*, including microglia and peripheral myeloid cells. Notably, bone marrow-derived peripheral myeloid cells are continuously replenished by newborn $CX3CR1^{+}$ cells, leading to almost complete renewal of the initially *Elf1*-knockout macrophage population within 30 days. In contrast, microglia undergo self-renewal and retain *Elf1* ablation lifelong (Supplemental Figure 12A).

To verify the efficiency of removing microglial *Elf1*, on day 35 after tamoxifen administration, we used FACS to isolate microglia ($CD45^{int}CD11b^{+}TMEM119^{+}$), other brain cells ($CD45^{-}CD11b^{-}$), and circulation myeloid cells ($CD45^{+}$ $CD11b^{+}$). As expected, quantitative analysis of *Elf1* mRNA in these FACS-isolated microglia showed that *Elf1* was virtually eliminated in microglia, whereas *Elf1* expression was unaffected in macrophages and other brain cells (Supplemental Figure 12, B and C).

To confirm the protective functions by which *Elf1*-cKO after TBI, we performed bulk RNA-seq and compared the differences between purified microglia 3 days after TBI (Figure 6A). Ablation of *Elf1* induced upregulation of anti-inflammation related genes such as *Arg1*, *Tgfb1*, *Lyz2*, and *Sall1* in microglia, while inflammation related genes such as *Tnf*, *Ccl2*, *Nlrp3*, *Il1b* and *Casp1* were downregulated (Figure 6, B and C). In additional, ablation of *Elf1* mediated the down-regulation of the inflammatory signaling pathway, the MAPK signaling pathway, and the NF-κB signaling pathway in aged and young microglia (Figure 6, D and E), and downregulated the proportion of $NLRP3^+$ microglia and upregulated the proportion of $Lysozyme^+$ microglia after TBI (Supplemental Figure 12, D-G).

To further characterize the inflammatory signature of *Elf1*-deficient microglia, we compared our TBI-induced DEG dataset with pro- and anti-inflammatory markers from the public database GSE69607. This analysis revealed that *Elf1*-ablated microglia exhibited a distinct inflammatory profile post-TBI, with reduced pro-inflammatory gene expression and elevated anti-inflammatory gene expression (Figure 6F). qRT-PCR confirmed the pro-inflammatory markers (*Il1b*, *Il6*, and *Tnf*) were downregulated and anti-inflammatory markers (*Il4*, *Il10*, and *Tgfb1*) were upregulated in cKO-TBI compared to WT and Cre controls (Figure 6, G and H). Modulation of the inflammatory response brought about significant improvements in survival and behavioral performance, as evidenced by a significant decrease in mortality in aged TBI mice, a decrease in mNSS scores and a prolongation of the latency to fall from the rotarod test (Figure 6, I-K).

6. Targeting ELF1 with Imeglimin confers neuroprotection in TBI

Currently, there are no commercially available ELF1 inhibitors. Therefore, we performed a structure-based high-throughput virtual screening (HTV) of 8561 compounds approved by the FDA or already in clinical use for potential ELF1 inhibitors. After successive SP and XP docking analyses, the 200 compounds with the highest docking scores were selected. After comprehensively analyzing the molecular weight, lipid solubility, and affinity to protein components in the blood-brain barrier of the 200 compounds, we screened the 10 compounds most likely to cross the blood-brain barrier for subsequent experiment (Figure 7, A and B).

Among all 10 alternative compounds, Imeglimin, a newly marketed antidiabetic agent with good safety profile (23), showed the strongest inhibitory effect on $NLRP3^+$ microglia formation (Figure 7C, and Supplemental Figure 13, A-D). Molecular docking showed that Imeglimin binds to the ATP pocket of the ELF1 protein through three hydrogen bonds (H-bonds) formed with VAL286, GLN283, and LYS279 (Figure 7D). Imeglimin modulated mitochondrial dysfunction of microglia, and improved the aerobic respiration of microglia which indicated by decreasing the ECAR and increasing the OCR (Figure 7, E and F). Based on a study of Imeglimin against ischemic brain injury, we determined the in vivo therapeutic concentration of Imeglimin to be 135 μg/kg/day (24). After in-vivo treatment at a concentration of 135 μg/kg for 7 days, Imeglimin increased the survival rate of mice with TBI within 45 days (Figure 7, G and H), decreased the proportion of $NLRP3^+$ microglia in the brain after injury (up-regulated the proportion of $Lysosome^+$ microglia) (Supplemental Figure 14, A-D). Imeglimin improved the neurological recovery and decreased the concentrations of pro-inflammatory cytokines IL-6 and IL-1β in the cerebrospinal fluid of mice after TBI (Figure 7, I-K). Interestingly, Imeglimin treatment reduced lymphocytes burden in the brains of TBI mice and decreased the transcription

of senescence-related markers Cdkn1a and Cdkn2a in microglia (Supplemental Figure 15, A-D).

To better understand Imeglimin functions by blocking ELF1 rather than off-target effects. We constructed three different HMC3 cell lines (wild type (WT), *ELF1*-knockout (KO), *ELF1*-knockout with Imeglimin treatment (KO+Ime)) and performed in vitro TBI modeling (Supplemental Figure 16A). Administration of Imeglimin in *ELF1*-KO microglia did not continue to reduce the proportion of $NLRP3^+$ microglia and did not improve ECAR and OCR in *ELF1*-KO microglia (Supplemental Figure 16B, E-F). To further explain the issue, we proceeded to construct three different HMC3 cell lines [wild-type (WT), *ELF1*-overexpressing (OE), *ELF1*-overexpressing with Imeglimin treatment (OE+Ime)] (Supplemental Figure 16C). The proportion of $NLRP3^+$ microglia was significantly elevated after *ELF1*-OE, whereas Imeglimin reversed this result and achieved a significant improvement even compared to WT control, administration of Imeglimin in *ELF1*-OE group significantly restored microglial aerobic respiration with improved ECAR and OCR (Supplemental Figure 16D, G-H). Finally, the results of the in vivo experiments corroborated the findings from the in vitro experiments. That is, after *Elf1*-cKO, Imeglimin could not further reduce the proportion of $NLRP3^+$ microglia in the brain after TBI (Supplemental Figure 16, I and J). The above findings could support that Imeglimin exerts its pharmacological effects mainly through blocking ELF1 rather than off-target effects.

Regarding the safety of Imeglimin treatment, we found Imeglimin did not cause decrease in blood glucose of sham mice, and the rise in blood glucose after TBI was suppressed by Imeglimin treatment (Supplemental Figure 17A). Except for blood glucose, Imeglimin

368 treatment did not cause blood pressure fluctuations in TBI mice (Supplemental Figure 17, B
369 and C). Histologic sections of each major organ did not indicate obviously toxicological effects
370 (Supplemental Figure 17D).
371

Discussion

In this study, we used scRNA-seq to reveal the characteristics of the brain immune microenvironment in the acute phase of TBI in aged and young mice. Myeloid immune responses dominated the acute phase after TBI, and were particularly severe in aged mice, among all myeloid immune cells, the number and proportion of microglia showed significant differences between aged and young mice after TBI. After downscaling the aggregates of microglia from different samples, we identified the two clusters of microglia most associated with the prognosis of TBI, the *Nlrp3*$^{+}$ cluster (worsening prognosis, higher prevalence in the aged) and the *Lyz2*$^{+}$ cluster (improving prognosis, higher prevalence in the young). Although we have validated the findings in the brain tissues from young and aged TBI patients, the small sample size as well as the heterogeneity of injury severity, treatment, tissue sampling, sample processing, and many other factors may confound the results. In addition, peripheral immune cells respond to chemokines and infiltrate the brain after TBI. Previous studies have shown that T cells and neutrophils interact with microglia and worsen TBI prognosis (25-28). These microglia subpopulations are disease-specific and are defined in the context of a comprehensive set of considerations, including spatiotemporal context, metabolic profile, and biological function.

Furthermore, several markers could provide a glimpse of the potential functions of *Nlrp3*$^{+}$ and *Lyz2*$^{+}$ microglia. Specifically, *Nlrp3* may promote the inflammatory response after TBI, whereas *Cst7* and *Spp1* which highly expressing in the *Lyz2*+ microglia are widely recognized in stage2 DAM to inhibit neurodegeneration by enhancing microglia phagocytosis (15). The heterogeneity of regional microglia is increasingly recognized using NLRP3 (*Nlrp3*$^{+}$) and

Lysozyme (*Lyz2*$^{+}$) labeling, which was confirmed by immunofluorescence staining to localize these two clusters of microglia around the injured area. For example, proliferative zone-associated microglia (PAM) have been found in developing white matter and white matter-associated microglia (WAM) in aged white matter (29, 30). In Alzheimer's disease, DAM surround amyloid plaques and persistently phagocytose amyloid-β aggregates (31). Understanding the regional heterogeneity of microglia and their functions may provide important clues for developing new therapies for different neurological diseases. Recently, numerous reports have shown that the M2 markers *Mrc1* (encoding CD206) and *Arg1* are predominantly expressed in borderline-associated macrophages (BAMs), but not in microglia (13, 32). Furthermore, the M1/M2 paradigm focuses only on inflammation, neglecting other important biological functions as well as the spatial heterogeneity of microglia. Our proposed *Nlrp3*$^{+}$ and *Lyz2*$^{+}$ microglia further negate the M1/M2 paradigm for post-TBI microglia.

Microglia stimulated by different microenvironments also showed different metabolic profiles. Several metabolic pathways related to amino acids and ketone bodies were enriched in *Lyz2*$^{+}$ microglia compared to the higher level of lipid metabolism in *Nlrp3*$^{+}$ microglia. Metabolism of branched-chain amino acids is thought to be neuroprotective by blocking microglia-mediated pro-inflammatory responses (33, 34). Glycolysis or interruption of the TCA cycle promotes a pro-inflammatory response in microglia, whereas an intact TCA cycle and OXPHOS maintain microglia dynamic homeostasis and inhibit excessive inflammation. In this study, aging significantly promoted glycolysis and inhibited TCA in microglia. in contrast, when *ELF1*, a key TF in *Nlrp3*$^{+}$ microglia, was knocked down, glycolysis was inhibited and TCA cycling was restored to ensure energy supply.

Epigenetic modifications can regulate gene expression without altering the genomic sequence (35, 36). The human epigenome is extremely dynamic and constantly changing in response to environmental exposures and the aging process. Differences in chromatin accessibility between aged and young microglia may be an important cause of differences in microglia profiles after TBI. In this study, we connect aging-enhanced glycolysis with enhanced aging-induced inflammatory responses in microglia through ATAC-seq. Using the SCENIC algorithm and Motfit enrichment, combining with the in-vitro CRISPR/Cas9 screening system, we identified a group of TFs (*ELF1*, *NFKB2*, *RELA*, *FLI1*, *NFKB1*, *JUN*, *JUNB*, and *FOSB*) capable of regulating the generation of *Nlrp3*$^{+}$ microglia, with *ELF1* ablation having the greatest effect on the generation of *Nlrp3*$^{+}$ microglia. Unfortunately, we did not identify the specific class of chromatin modifications that lead to chromatin opening, which requires subsequent experiments to provide evidence. Previous studies have shown that *ELF1* binds to the NIS-lncRNA promoter to upregulate CCL2 expression and thus induce pathological pain (37). In this study, ablation of *ELF1* in microglia in vivo significantly inhibited the flux of inflammation-related signaling pathways (MAPK and NF-κB signaling pathways) and reduced the transcription of pro-inflammatory cytokines. The inflammation-suppressing effect of ablation of *ELF1* represents its broad-spectrum initiating effect on pro-inflammatory cytokines.

Imeglimin targets cellular mitochondrial dysfunction and is a novel oral hypoglycemic agent with dual mechanisms (18, 38). In this study, we found the novel function of Imeglimin, as an inhibitor of ELF1 that can cross the blood-brain barrier and thereby reduce the population of *Nlrp3*$^{+}$ microglia after TBI. Treatment carried out at a concentration of 135 μg/kg did not cause fluctuations in blood pressure of Sham or TBI mice. The results of histological sections

of the lungs, liver, spleen, kidneys and heart under different conditions of Imeglimin treatment are also not suggestive of organ toxicity, which reflects the safety of Imeglimin. Excessive elevation of blood glucose after TBI is thought to be negatively correlated with the prognosis of TBI, aging-induced enhancement of microglial glycolysis will lead to a decrease in the ability of microglia to process glucose, and accumulation of oxygen free radicals induced by high glucose further aggravates the elevation of inflammation in microglia, which could be well ameliorated by the pharmacological effect of Imeglimin through blocking ELF1 (39-41). As an FDA-approved and marketed drug (18), Imeglimin has the potential to be used in the treatment of TBI, but more preclinical evidence remains to be provided.

A critical limitation of our study is the lack of age-matched non-TBI human brain tissues as control. This absence prevents us from definitively distinguishing between age-related baseline differences in microglial phenotypes and changes specifically induced by TBI in human subjects. For instance, we cannot fully rule out whether the higher proportion of *Nlrp3*$^{+}$ microglia or lower abundance of Lyz2^{+} microglia observed in aged TBI patients reflects a pre-existing age-associated shift in microglial homeostasis, rather than a direct response to traumatic injury. Despite these limitations, our integrative multi-omics approach and cross-species validation provide convergent evidence linking age, microglial heterogeneity, metabolic-epigenetic crosstalk, and TBI outcomes, laying the foundation for future therapeutic interventions targeting ELF1-mediated microglial dysfunction.

Methods

Sex as a biological variable

Our study examined male and female animals, and similar findings are reported for both sexes.

Human brain samples

Human studies were conducted in accordance with the Declaration of Helsinki. Inclusion of human subjects and supporting documentation were approved by the Ethics Committee of Nantong University Affiliated Hospital (Approval No. 2023-K187-01). Informed consent of all subjects or legal representatives was obtained at enrollment. Contusion brain tissue was obtained from moderate to severe TBI patients undergoing hematoma evacuation and decompression craniotomy. We obtained brain tissues from the contused area of TBI patient who underwent surgery within 24 hours, which included both gray and white matter, with a tissue size of approximately 1-3 cm^3.

Brain tissue was minced and enzymatically dissociated into single cell suspensions using a papain-based neural tissue dissociation kit. After centrifugation in 30% Percoll to remove myelin debris, single cells were suspended in 1% bovine serum albumin.

A total of 13 young (＜60 years old) and 22 aged (>65 years old) subjects were included in the study. Patient characteristics are provided in Supplemental Table 1 and Supplemental Table 2.

Mice

C57BL/6J-*Elf1*^{em1flox} (*Elf1*$^{fl/fl}$), C57BL/6J-*Nlrp3*^{em1flox} (*Nlrp3*$^{fl/fl}$) and C57BL/6J-*Lyz2*^{em1flox}

(*Lyz2*$^{fl/fl}$) mice were purchased from Cyagen Biosciences. C57BL/6-*Cx3cr1*$^{em1(creERT2\text{-}WPRE\text{-}polyA)}$ (*Cx3cr1*^{creERT2}) mice were purchased from Shanghai Model Organisms Center. B6.Cg-*Gt*(ROSA)26Sor$^{tm9(CAG\text{-}tdTomato)Hze}$/J (Ai9 reporter mice) was kindly given by Professor Yang Yang. Young (6-8 weeks) and old (16-18 months) wild-type C57BL/6 mice were either bred and aged in house, or purchased from Chengdu Dossy Experimental Animals Co., Ltd. All mice used in this study were not sex-specified. Experimental mice were kept in an air-conditioned room (Temp: 22–25 °C) with standard 12 h of light/dark cycles and free access to food and water. The National Institutes of Health of the United States Guide for the Care and Use of Laboratory Animals was followed for all animal experiments. The experimental procedures used in this study were approved by the Experimental Animal Ethics Committee of Nantong University (Approval No. IACUC20231125-1001).

Mice genotyping

Tail specimens (0.2–0.5 cm in length) were harvested from 2-week-old mice using sterile surgical scissors sanitized with 70% ethanol. Genomic DNA was isolated following the standard protocol of the Beyotime Mouse Tail Genotyping Kit (D7283M). Subsequent to DNA extraction, polymerase chain reaction (PCR) was carried out with specific primer sets, and the resulting PCR amplicons were subjected to electrophoresis on a 2% agarose gel impregnated with GelRed™ (Biotium) at 120 V for 30 minutes. The molecular weights of the target bands were verified by comparison with the DL2000 DNA ladder (Takara).

Elf1$^{flox/flox}$: Forward primer: 5′-GCTGCTGAAGATGCTGATGG-3′ and reverse primer: 5′-GGATGGTGGTGAAGGTGAAG-3′ yield a 394 bp product for floxed alleles and a 320 bp

product for WT alleles. *Cx3cr1-Cre*$^{ki/wt}$: Forward primer: 5′-TGGCTGCTGCTGTTGTTGTA-3′ and reverse primer: 5′-CAGAGACGGAAATCCATCGCT-3′ amplifies a 428 bp knock-in (KI) product and a 286 bp WT product.

TBI model

TBI was induced in mice using the controlled cortical injury (CCI) model. Briefly, anesthesia was induced and maintained in mice using isoflurane, and then the heads of mice were fixed in a stereotaxic frame, and a heat pack was placed under the body to maintain body temperature. A midline incision was made on the scalp, and a 2 mm-diameter bone window was created 2.0 mm lateral to the median sagittal line and 1.0 mm posterior to the bregma. The brain was tilted at a 15° angle and perpendicular to the impactor (4-mm diameter tip; RWD Life Sciences, China). The impactor parameters for CCI were impact velocity, 3.5 m/s; deformation depth, 1.30 mm; and duration, 400 ms. After CCI, the skin incision was sutured and treated with antibiotic ointment to prevent infection. Finally, the mice were placed on a heating pad to maintain core body temperature until they recovered from anesthesia. For the sham group, craniotomy was performed and the dura was exposed, but no impact was performed.

Repeat mild traumatic brain injury (rmTBI) model

For the repetitive mild traumatic brain injury (rmTBI) model was established as described previously. Briefly, mice were induced and maintained under anesthesia using isoflurane. The mice were subsequently shaved on the head and the head was immobilized in the stereotaxic apparatus. A heating pad was placed under the torso to maintain body temperature, and non-

invasive rubber pads were fixed on both sides of the head to prevent lateral displacement during impact. The tip of a 5-mm blunt-ended metal impactor was positioned above the sagittal suture before each impact. Impacts were applied to the intact skulls at an impact velocity of 5 m/s, a strike depth of 1.0 mm, and a dwell time of 200 ms, a condition in which the instantaneous impact force applied to the head of the mice was approximately 72 N. All mice experienced transient apnea (<20 seconds) and no skull fractures were observed. After surgery, the mice were placed on a heating pad until they regained voluntary movement and were subsequently returned to their cages and provided with soft chow and water. rmTBI group mice were subjected to the injury procedure at a frequency of 1 per day at 24-hour intervals (5 times per week, Monday through Friday), for a cumulative total of 20 impacts. To control for repeated anesthetic effects, mice in the sham-operated group received the same anesthetic regimen but were not subjected to the impingement procedure. The health status and behavioral abnormalities of the mice were monitored daily throughout the injury protocol and in the postoperative period.

In-vitro TBI model

The establishment of the in vitro TBI model was performed as previously described (42). Briefly, SH-SY5Y human neuroblastoma cells were differentiated into neurons using combined retinoic acid and BDNF induction according to established protocols (43), followed by needle scratch injury manipulation. Simultaneously, microglia (2×10^5 cells per insert of 12-well inserts) were cultured in the transwell upper permeable insert (3-mm-diameter pores, Corning, REF3402). The original DMEM/F12 media (with 10% FBS) for the microglia was gradually

replaced with a mixture of Dulbecco's Modified Eagle Medium and Ham's F12 supplemented with 10% fetal bovine serum (FBS) and 1% penicillin/streptomycin with a ratio change over slowly (50:50, 25:75, 0:100) to allow the cells to acclimate to the difference in nutrient content and remain in a relative resting condition. After 48 hours, the microglia-containing inserts were transferred to the upper chambers of neuron culture plates subjected to needle scratch injury and activated for 24 hours. Subsequent procedures were then performed.

Flow cytometry

Mice were euthanized using isoflurane lethal anesthesia, and the brains were removed. The brains were minced and enzymatically digested into a single cell suspension using a papain-based nerve tissue dissociation kit. Myelin fragments were subsequently removed by centrifugation in 30% Percoll, and single cells were suspended in 1% bovine serum albumin for antibody staining. For human samples, antibody staining was performed after obtaining single-cell suspensions as described previously. Microglia were sorted with flow cytometry after staining with anti-CD11b and CD45 antibodies. The purity of microglia ($CD11b^{+}$ $CD45^{int}TMEM119^{+}$) is about 99% assessed by flow cytometry. The antibodies used are listed in the antibody list in Supplemental Table 3. Data were collected by a BD LSRFortessa SORP flow cytometer and analyzed using FlowJo software.

Total RNA extraction and quantitative real-time polymerase chain reaction (qRT-PCR)

Microglia from the contused brain tissue of TBI patients or the injured cerebral hemisphere of TBI mice were sorted according to the flow cytometry gating strategy described above. Total

RNA was extracted from brain tissue or microglia using the FastPure Cell/Tissue Total RNA Isolation Kit V2 (Vazyme Biotech Co., Ltd., Nanjing, China). Subsequently, reverse transcription of 1000 ng of extracted total RNA was performed using a reverse transcription kit (Thermo Fisher Scientific, Waltham, MA, USA). Tissue and cell complementary DNAs were diluted 20-fold and 10-fold, respectively, in preparation for subsequent assays. qRT-PCR was performed using Q5 (Thermo Fisher Scientific), and *ACTB* (*Actb*) was used as an internal reference for messenger RNA. The polymerase chain reaction primer sequences are provided in Supplemental Table 4. Analysis was performed using the $2^{-\Delta\Delta CT}$ method.

Bulk RNA sequencing

Total RNA was extracted from purified microglia isolated from the ipsilateral cerebral hemisphere 3 days after TBI using the RNeasy Mini Kit (Qiagen) following the manufacturer's instructions. The concentration and purity of the RNA were assessed using a NanoDrop 2000 spectrophotometer (Thermo Fisher Scientific), and the integrity was evaluated with an Agilent 2100 Bioanalyzer (Agilent Technologies). Only RNA samples with an RNA Integrity Number (RIN) greater than 7.0 were used for library preparation. Libraries were prepared with Illumina TruSeq RNA Library Prep Kit v2. After library QC and quantification via Qubit quantification (ThermoFisher, Waltham, MA), RNA Sequencing was carried out on an Illumina NextSeq 2000 with paired end. FASTQ files were mapped to mm10 (GRCm38.p6) mouse genome and gene counts were obtained with STAR version 2.7.2b. Differential gene expression analysis was performed using R package DESeq2.

590 Immunofluorescence staining

591 Following euthanasia of mice with isoflurane overdose, cardiac perfusion was sequentially
592 performed using cold PBS for blood clearance, followed by 4% paraformaldehyde (PFA)
593 perfusion for tissue fixation. After brain extraction, post-fixation was conducted with 4% PFA,
594 followed by dehydration in 30% sucrose and embedding in OCT compound (Tissue-Tek) for
595 storage at -20℃ until further processing. For contused brain tissues from TBI patients, surgical
596 specimens were immediately immersed in 4% PFA for fixation, then subjected to dehydration
597 and embedding procedures as described above.

598 Human and mice brain tissues were sectioned into 10-μm-thick slices using a microtome
599 (Leica), and then were used for immunofluorescence staining. Five sections per tissues, peri-
600 lesional site were selected. Antigen retrieval was performed using Quick Antigen Retrieval
601 Solution for Frozen Sections (Beyotime, P0090) for 30 minutes. After PBS rinsing, sections
602 were blocked with 5% normal donkey serum (Jackson Nutrition) in PBS for 2 hours, followed
603 by staining and overnight incubation at 4℃. After secondary antibody incubation, nuclei were
604 counterstained with 4',6-diamidino-2-phenylindole (C0060, Solarbio), and slides were mounted
605 using anti-fade mounting medium (S2100, Solarbio). Immunofluorescence images of mouse
606 injured hemispheres or human brain tissues were acquired at 10× or 20× magnification using
607 the navigated imaging function of a Leica Thunder 3D Assay inverted fluorescence microscope,
608 with subsequent panoramic tissue reconstruction performed via LASX software. Fiji (ImageJ)
609 software was employed for image processing and quantitative analysis of the peri-lesional
610 cortex, including calculations of cellular coverage area and cell counts.

611

612 Intracerebroventricular viral injection

613 Adeno-associated viral vectors [rAAV-m*Cx3cr1-Cre*-WPRE-SV40pA (AAV-*Cx3cr1-Cre*) and
614 rAAV-m*Cx3cr1*-WPRE-SV40pA (AAV-*Cx3cr1*), AAV2/MG1.2, 2.00E+12vg/mL] (PackGene
615 Biotech, Guangzhou, China) were injected into the right cortex (Point 1: 1.7 mm posterior, 1
616 mm lateral (right), and 1.0 mm ventral relative to bregma; Point 2: 1.7 mm posterior, 2 mm
617 lateral (right), and 1.0 mm ventral relative to bregma). The injection volume was 0.5 μL for
618 each point at the rate of 0.25 μL/min, and the needle was left in the brain for 5 min after injection
619 to prevent leakage. The burr hole was closed with bone wax, and the incision was closed with
620 sutures. Mice were placed in separate recovery cages. TBI models were established after the
621 viral growth reached its peak on day 28.

622

623 Cell culture

624 SH-SY5Y human neuroblastoma cell line and HMC3 human microglia cell line were purchased
625 from BeNa Culture Collection (BNCC, China), and cells were cultured in DMEM/F12
626 containing 10% FBS and 1% penicillin/streptomycin in an incubator with 37°C/5% CO2.

627

628 Seahorse assays

629 Microglia were collected from mice brain tissue by fluorescence-activated cell sorting (FACS).
630 Purified microglia were cultured in DMEM/F12 containing 10% FBS and 1%
631 penicillin/streptomycin in an incubator with 37°C/5% CO2. Cultured plates were used to plate
632 $5x10^5$ microglia sorted from mice brain or from different groups of HMC3 cell lines.
633 Extracellular Acidification Rate (ECAR) and Oxygen Consumption Rate (OCR) was measured

using an XF24 Seahorse Extracellular Flux Analyzer following the manufacturer's instructions. In the seahorse assays, microglia were treated with glucose (10 mM), oligomycin (1.5 μM), and 2-deoxy-D-glucose (2-DG; MCE, HY-13966; 50 mM) for ECAR, and oligomycin (0.25 mM), FCCP (0.25 mM), rotenone (0.25 mM) and antimycin A (0.25 mM) for OCR. Each condition was performed with 3 replicates.

Evaluation of neurological deficit

Neurological function assessment was independently performed by two investigators who were blinded to treatment assignment. Neurological deficits in mice were assessed using the modified Neurological Scale Score (mNSS), which comprehensively evaluates motor, sensory, reflex and balance functions through a battery of tests. Detailed scoring information are provided in Supplemental Table 5. Scores for mice range from 0 to 18; 13 to 18 indicates severe injury, 7 to 12 indicates moderate injury, and 1 to 6 indicates mild injury.

Rotarod test

Mice were trained on an accelerated (5-30 rpm) rotarod for 3 days. During the test phase, mice were placed on an accelerating rotary rod with the speed increasing from 5 rpm to 30 rpm over 5 min. The latency of mice to fall from the rod was recorded, and each mouse was trained for 5 trials (each trial run for 5 min, rest for 5 min). The final score is the average latency of the 5 falls of the experimental mice. Rotarod testing was performed 30 days after TBI. All experiments and data analyses were performed in a blinded manner.

Virus infection

The construction of vectors and retroviral packaging were assisted by Packgene Biotech (Guangzhou, China). Virus overexpression *ELF1* was also purchased from Packgene Biotech. First, Cas9 protein fused with GFP fluorescent tag was transfected into HMC3 cells using lentivirus. Then, the successfully transfected HMC3-Cas9-GFP cells were mixedf with HMC3 cells at a ratio of 3:7. In the presence of 8 μg/ml polybrene (Beyotime, C0351), the retrovirus was transduced at 1260g for 90 minutes at 32°C to infect HMC3 cells. After 6 hours, the culture medium was removed and replaced with fresh culture medium. Three sgRNA plasmids were constructed for each target gene, and the sgRNA with the highest editing efficiency and editing rate of more than 50% for each target gene was selected for screening. The screened sgRNA sequences and editing efficiency in HMC3 cells are listed in Supplemental Table 6.

Compound screening for ELF1

Downloading the 3D structure of Human elf1 from the AlphaFold website (AlphaFold ID: AF-P32519-F1) from the AlphaFold website, the DNA binding domain was intercepted and the protein was hydrogenated using the Protein Preparation Wizard module. This was followed by energy optimization (OPLS2005 force field, RMSD of 0.30 Å). The processed proteins were used to create a grid file using the Receptor Grid Generation module to generate a grid file centered on the key amino acids LEU268/VAL286/TYR287, with the box size set to 20 Å × 20 Å × 20 Å. The 2D formats of HY-L022P FDA-approved Drug Library Plus (containing 3230 compounds) and HY-L035P Drug Repurposing Compound Library Plus (containing 5331 compounds) were processed through the LigPrep module of the Schrödinger software for

hydrogenation, energy optimization, etc., and the 3D structures were outputted for virtual screening.

Virtual screening was carried out using the Virtual Screening Workflow module. The prepared compounds were imported, and molecular docking was performed using the Glide module. Molecular docking refers to the mutual docking between receptor and ligand molecules through geometric and energy matching.: First, use the standard (SP) mode in the Glide module to screen the prepared small - molecule compounds from HY-L035 Drug Repurposing Compound Library Plus (MedChemexpress). Select the top 10% of small - molecule compounds with the highest scoring values and conduct a second - round screening using the high - precision (XP) mode to obtain the ranking of the small - molecule compounds.

Finally, we calculated the possibility of crossing the blood-brain barrier based on the lipid solubility, molecular weight of the compounds. And the top ten compounds were selected for validation based on the absolute value of docking score.

Drug administration

Tamoxifen (HY-13757A, MedChemExpress) was dissolved in ethanol/corn oil (1:9) at a concentration of 30 mg/ml, and Cx3cr1$^{creERT2/wt}$; *Elf1*$^{Flox/Flox}$ mice received 100 μl (3 mg per mouse) daily for three consecutive days by intraperitoneal injection. Imeglimin (HY-14771A, MedChemExpress) was dissolved in 10% dimethyl sulfoxide (DMSO) and 90% corn oil. Mice received intraperitoneal injections of 150ug/kg/day imeglimin or equal volumes of solvent. Injections of imeglimin or vehicle were started on the day after TBI and continued for 7 consecutive days. The MCC950 was purchased from MedChemExpress (HY-12815).

Detection of cytokine concentrations and blood glucose in serum

Serum levels of IL-6 and IL-1β in mice were measured using commercial ELISA kits according to the manufacturer's instructions. The ELISA kits used are listed below: Mouse IL-6 ELISA Kit (Multi Sciences, EK206), Mouse IL-1β ELISA Kit (Multi Sciences, EK201B).

Serum levels of glucose in mice were measured using glucose Fluorometric Assay Kit (Multi Sciences, E-BC-F037) according to the manufacturer's instructions.

Measurement of mice blood pressure

Blood pressure was assessed in mice using the BP-2000 Blood Pressure Analysis System (Visitech Systems, USA) through tail-cuff transmission photoplethysmography. Briefly, mice were placed in a restraint device allowing tail passage through a cuff equipped with optical sensors. The standard test session was run for 20 times and systolic blood pressure (SBP), diastolic blood pressure (DBP), and heart rate parameters were acquired.

Preparation of single cell suspensions from mouse cerebral hemisphere

Fresh mouse cerebral hemispheres were rinsed in sterile phosphate-buffered saline (PBS) to remove blood and debris. The tissue was then finely minced with sterile scissors and forceps to increase the surface area for enzymatic digestion. The minced tissue was digested enzymatically by incubating it with 0.05% Liberase TL (Roche) in PBS at 37°C with gentle shaking for 15-30 minutes. After digestion, the tissue was mechanically dissociated by passing it through a 40 μm sterile nylon mesh to generate a single-cell suspension. This suspension was centrifuged at

300g for 5 minutes to pellet the cells, which were subsequently resuspended in sterile PBS or culture medium. The cell suspension was then filtered through a 40 μm cell strainer to remove any remaining debris or clumps. Cells were counted using a hemocytometer or automated cell counter, and viability was assessed with Trypan Blue staining. The resulting single-cell suspension was either used immediately for downstream applications, stored at 4°C for short-term use, or frozen with a cryoprotectant for long-term storage.

Single-cell RNA-sequencing library preparation and sequencing

Single-cell RNA-sequencing was conducted by Shanghai GeneChem Co., Ltd. In brief, cell suspensions were processed to generate single-cell RNA-Seq libraries using the Chromium Next GEM Single Cell 5′ GEM, Library, and Gel Bead Kit v3.1 (10x Genomics, Pleasanton, CA, USA) according to the manufacturer's protocol, as outlined below. Briefly, cell samples (16,500 cells per sample) were loaded into a Chromium Single-Cell Instrument (10x Genomics, Pleasanton, CA, USA) to generate single-cell Gel Bead-in-Emulsions (GEMs), targeting the capture of 10,000 cells per sample. Reverse transcription within GEMs (GEM-RT) was performed to synthesize barcoded full-length cDNA from polyadenylated mRNA. After GEM disruption, the GEM-RT reaction mixtures were pooled, and cDNA was purified using silane magnetic beads (DynaBeads MyOne Silane Beads, Thermo Fisher Scientific). The purified cDNA was then amplified by PCR, followed by enzymatic fragmentation and size selection to optimize cDNA amplicon size. Indexed sequencing libraries were constructed through end repair, A-tailing, adaptor ligation, and PCR amplification. The final libraries, containing P5 and P7 priming sites for Illumina bridge amplification, were sequenced on an Illumina NovaSeq

6000.

Single-cell RNA-sequencing data analysis

All single-cell RNA analysis was performed in R (version 4.0.2) using the Seurat package (version 4.1.1). Cells with fewer than 200 detected genes, more than 5,000 detected genes, or over 10% mitochondrial gene content were filtered out to remove low-quality or apoptotic cells. Data normalization was performed using Seurat's NormalizeData function, employing a log-normalization method to account for differences in sequencing depth. The FindVariableFeatures function was used to identify highly variable genes, followed by data scaling with the ScaleData function, which regresses out unwanted sources of variation such as total UMI counts and mitochondrial content. We applied the Harmony algorithm using the RunHarmony function to integrate samples. Dimensionality reduction was carried out using Principal Component Analysis (PCA) through the RunPCA function, which reduced the dataset's dimensionality while retaining key variation. For clustering, the shared nearest neighbor (SNN) modularity optimization-based algorithm was applied using the FindNeighbors and FindClusters functions, typically with a resolution parameter tuned to optimize cluster granularity. Clusters were visualized using Uniform Manifold Approximation and Projection (UMAP) via the RunUMAP function, providing a two-dimensional representation of the cellular landscape. Differential expression analysis was performed with the FindMarkers function, which typically uses the Wilcoxon rank-sum test to identify genes that are differentially expressed between clusters. The SCENIC transcription factor inference was performed using the package SCENIC (v1.2.4) following the recommended guideline. The AddModuleScore function in Seurat was utilized to

calculate the scores for the genes of interest. Gene Set Variation Analysis (GSVA) was employed to assess the enrichment of various pathways across different cell populations by transforming the gene expression matrix into a gene set expression matrix for these populations. Based on the pathway activity scores obtained for each cell through GSVA, differential tests were conducted to compare the pathway activity scores of each cell group against those of all other cell groups.

SCENIC analysis

We employed SCENIC (v1.2.4) to delineate the transcription factors (TFs) regulating microglia population formation. SCENIC identifies regulons, comprising TFs and their potential target genes, for each cell population and quantifies their activity. The regulon activity level serves as an indicator of the TF's influence within the cell, with elevated activity reflecting a stronger regulatory impact. The SCENIC workflow involved running the following steps: 'runSCENIC_1_coexNetwork2modules' to infer the gene regulatory network (GRN), 'runSCENIC_2_createRegulons' to predict regulons using RcisTarget databases, 'runSCENIC_3_scoreCells' to score regulon activities, and 'runSCENIC_4_aucell_binarize' to cluster cells based on GRN activity.

Metabolomics LC-MS analysis

Metabolomics LC-MS analysis was conducted by Bionovogene Co., LTD. In brief, The ExionLC ultra-high performance liquid chromatography system (AB Sciex, USA) was operated on an Agilent Eclipse XDB-C18 (2.1 × 150 mm, 5 μm, Agilent, USA) column with an injection

volume of 5 μL, a column temperature of 40 °C, and mobile phases of a- 6.25 mm ammonium acetate (containing 0.2% acetic acid) and B- 0.2% acetic acid (containing methanol). The gradient elution conditions were 0-2 min, 20% B; 2-6 min, 20-70% B; 6-7 min, 70-20% B; 7-9.00 min, 20% b at a flow rate of 0.4 mL/min.

Mass spectrometry analysis was performed on an AB Sciex triple quadrupole 6500 + mass spectrometer (AB Sciex, USA) in multiple reaction monitoring (MRM) mode. Electrospray ionization (ESI) parameters in negative mode were: ion source voltage -4000 V; ion source temperature, 600 °C; curtain gas, 30 psi; gas 1,60 psi and gas 2,60 psi.

Bulk ATAC sequencing

ATAC-seq was conducted by Shanghai Jiayin Biotech. In brief, $NLRP3^{+}$ and $Lysozyme^{+}$ Microglia were sorted from mouse brain after TBI according to the flow cytometry gating strategy. Subsequently, the hierarchically folded DNA was simultaneously cleaved using Tn5 transposase. Native nuclei were purified using the MinElute PCR Purification Kit (Qiagen, 28004) and subjected to six cycles of quantitative real-time PCR amplification. 10 ng of genomic DNA was used as an input control. For data filtering, raw reads were processed using Trimmomatic (V0.35, http://www.usadellab.org/cms/?page=trimmomatic).

BWA software (https://bio-bwa.sourceforge.net/) was used for alignment. The fragment sizes of the read pairs were calculated using the BAM files from aligned paired-end sequencing data. Summary statistics of fragment lengths were estimated by sampling several regions based on the size of the genome and the number of processors. MACS2 (V2.2.7.1, https://pypi.org/project/MACS2/) was used for peak calling in this analysis, Bedtools (V2.30.0,

https://bedtools.readthedocs.io/en/latest/) were mainly used for peak annotation analysis. Transcription factor binding motifs were identified with HOMER findMotifsGenome.pl tool in the chromatin-accessible region; those with P-value <0.05 were considered significant.

Biological function enrichment analysis

Gene Ontology (GO) and Kyoto Encyclopedia of Genes and Genomes (KEGG) enrichment analyses were using the "clusterProfiler" R package, with a adj. $P<0.05$ serving as the filtering standard for functional analysis. The Gene Set Enrichment Analysis (GSEA) was performed by R packages "clusterProfiler" and "ggpolt2" were subsequently employed to analyze and visualize GSEA data. The significance of GSEA analysis enrichment was determined by threshold values (adj. $P<0.05$)

Statistical analysis

The data were analyzed utilizing GraphPad Prism 10.5.0 and subsequently expressed as the mean ± standard error of the mean. We used the Shapiro–Wilk test to assess the normality of the distribution of continuous variables. All data are tested for normality, and data that does not show a normal/Gaussian distribution is analyzed by nonparametric equivalents. Comparisons were made using the unpaired Student's t-test, one-way analysis of variance (ANOVA), and two-way ANOVA. Survival analysis was performed using the Kaplan–Meier method and compared by log-rank test. A P value less than 0.05 was considered significant. Each experiment was replicated a minimum of three times.

Study approval

The study was approved by the Ethics Committee of the Affiliated Hospital of Nantong University (Approval No. 2023-K187-01). All participants provided written informed consent. All experimental procedures were in accordance with the Guidelines on the Care and Use of Laboratory Animals and were approved by the Nantong University Laboratory Animal Ethics Committee (Approval No. IACUC20231125-1001).

Data availability

scRNA-seq data of mice brains could be available at Genome Sequence Archive (GSA) database under accession number CRA033293. All data values reported in this work are reported in the supporting data values file. The article and the supplemental material present all data needed to evaluate the conclusions.

Author contributions

Writing-original draft: ZCL, YS, CXW, ZHL, WS, KS, PPG. Conceptualization: ZCL, YS, ZHL, WS, KS, PPG. Investigation: ZCL, YS, CXW, ZHL, ZHW, QQL, RJ, JWZ, WQL, XJZ, JZ, YQZ. Writing-review & editing: ZCL, YS, CXW, ZHL, WS, KS, PPG. Methodology: ZCL, YS, CXW, ZHL, ZHW, QQL, RJ, WQL, XJZ, JWZ, JZ, YQZ. Resources: WS, KS, PPG. Funding acquisition: WS, KS, PPG, QQL. Data curation: ZCL, YS, CXW, ZHL, ZHW, QQL, RJ, WQL, XJZ. Validation: ZCL, YS, CXW, ZHL, ZHW, QQL, RJ, WQL, XJZ, JWZ, WS, KS, PPG. Supervision: WS, KS, PPG. Formal analysis: ZCL, YS, CXW, ZHL, WS, KS. Software: YS, ZHL, ZHW, JWZ. Project administration: WS, KS, PPG. Visualization: ZCL, YS, CXW, ZHL, ZHW, JWZ. All authors have read and agreed to the published version of the manuscript. ZCL, YS, CXW and ZHL contributed equally to this study.

Acknowledgments

Our study was financially supported by the National Key Research and Development Program of China (2023YFC2306502 to WS), the National Natural Science Foundation of China (82471422, 82271415 to PPG), Fundation of Jiangsu Province Research Hospital (YIXYY202204-ZD15, YJXYY202204-ZD16, and YJXYY202204-XKB12 to WS), the National Natural Science Foundation of China (82301561 to QQL), the National Natural Science Foundation of China (82322023, 82101364 to KS), and the National Natural Science Foundation of China (82371398 to WS). We sincerely thank Professor Yang Yang for his kindness of providing B6.Cg-*Gt*(ROSA)26Sor$^{tm9(CAG\text{-}tdTomato)Hze}$/J (Ai9 reporter mice) for the revision. We thank Prof. Bin Wei, Prof. Hongyan Wang and Dr. Yingcheng Wu for their

guidance and assistance with this study.

Additional information

Supplemental Material includes 17 supplemental figures and 7 supplemental tables are available for this paper online.

References

1. Dams-O'Connor K, et al. Traumatic brain injury as a chronic disease: insights from the United States Traumatic Brain Injury Model Systems Research Program. *Lancet Neurol.* 2023;22(6):517-28.
2. Jiang JY, et al. Traumatic brain injury in China. *Lancet Neurol.* 2019;18(3):286-95.
3. Rosenfeld JV, et al. Early management of severe traumatic brain injury. *Lancet.* 2012;380(9847):1088-98.
4. Peeters W, et al. Epidemiology of traumatic brain injury in Europe. *Acta Neurochir (Wien).* 2015;157(10):1683-96.
5. Injury GBDTB, and Spinal Cord Injury C. Global, regional, and national burden of traumatic brain injury and spinal cord injury, 1990-2016: a systematic analysis for the Global Burden of Disease Study 2016. *Lancet Neurol.* 2019;18(1):56-87.
6. Urbanus J, et al. DRAG in situ barcoding reveals an increased number of HSPCs contributing to myelopoiesis with age. *Nat Commun.* 2023;14(1):2184.
7. Mann M, et al. Heterogeneous Responses of Hematopoietic Stem Cells to Inflammatory Stimuli Are Altered with Age. *Cell Rep.* 2018;25(11):2992-3005 e5.
8. Corps KN, et al. Inflammation and neuroprotection in traumatic brain injury. *JAMA Neurol.* 2015;72(3):355-62.
9. Yong HYF, et al. The benefits of neuroinflammation for the repair of the injured central nervous system. *Cell Mol Immunol.* 2019;16(6):540-6.
10. Antignano I, et al. Aging microglia. *Cell Mol Life Sci.* 2023;80(5):126.
11. Harry GJ. Microglia during development and aging. *Pharmacol Ther.*

2013;139(3):313-26.

12. Marschallinger J, et al. Lipid-droplet-accumulating microglia represent a dysfunctional and proinflammatory state in the aging brain. *Nat Neurosci.* 2020;23(2):194-208.

13. Silvin A, et al. Dual ontogeny of disease-associated microglia and disease inflammatory macrophages in aging and neurodegeneration. *Immunity.* 2022;55(8):1448-65 e6.

14. Chen Y, and Colonna M. Microglia in Alzheimer's disease at single-cell level. Are there common patterns in humans and mice? *J Exp Med.* 2021;218(9).

15. Deczkowska A, et al. Disease-Associated Microglia: A Universal Immune Sensor of Neurodegeneration. *Cell.* 2018;173(5):1073-81.

16. Borst K, et al. Microglia metabolism in health and disease. *Neurochem Int.* 2019;130:104331.

17. Lauterbach MA, et al. Toll-like Receptor Signaling Rewires Macrophage Metabolism and Promotes Histone Acetylation via ATP-Citrate Lyase. *Immunity.* 2019;51(6):997-1011 e7.

18. Lamb YN. Imeglimin Hydrochloride: First Approval. *Drugs.* 2021;81(14):1683-90.

19. Planas AM. Role of Immune Cells Migrating to the Ischemic Brain. *Stroke.* 2018;49(9):2261-7.

20. Li H, et al. Acute ischemia induces spatially and transcriptionally distinct microglial subclusters. *Genome Med.* 2023;15(1):109.

21. Rachmian N, et al. Identification of senescent, TREM2-expressing microglia in aging and Alzheimer's disease model mouse brain. *Nat Neurosci.* 2024;27(6):1116-24.

22. Li L, et al. Glis1 facilitates induction of pluripotency via an epigenome-metabolome-epigenome signalling cascade. *Nat Metab.* 2020;2(9):882-92.

23. Hagi K, et al. Efficacy, safety and tolerability of imeglimin in patients with type 2 diabetes mellitus: A meta-analysis of randomized controlled trials. *J Diabetes Investig.* 2023;14(11):1246-61.

24. Zemgulyte G, et al. Imeglimin Is Neuroprotective Against Ischemic Brain Injury in Rats-a Study Evaluating Neuroinflammation and Mitochondrial Functions. *Mol Neurobiol.* 2022;59(5):2977-91.

25. Kedia S, et al. T cell-mediated microglial activation triggers myelin pathology in a mouse model of amyloidosis. *Nat Neurosci.* 2024.

26. Shi SX, et al. CD4(+) T cells aggravate hemorrhagic brain injury. *Sci Adv.* 2023;9(23):eabq0712.

27. Rosenzweig N, et al. Sex-dependent APOE4 neutrophil-microglia interactions drive cognitive impairment in Alzheimer's disease. *Nat Med.* 2024.

28. Zhang Q, et al. Neuroinflammation in Alzheimer's disease: insights from peripheral immune cells. *Immun Ageing.* 2024;21(1):38.

29. Li Q, et al. Developmental Heterogeneity of Microglia and Brain Myeloid Cells Revealed by Deep Single-Cell RNA Sequencing. *Neuron.* 2019;101(2):207-23 e10.

30. Safaiyan S, et al. White matter aging drives microglial diversity. *Neuron.* 2021;109(7):1100-17 e10.

31. Wang X, et al. Intermittent hypoxia training enhances Abeta endocytosis by plaque associated microglia via VPS35-dependent TREM2 recycling in murine Alzheimer's

disease. *Alzheimers Res Ther.* 2024;16(1):121.

32. Ransohoff RM. A polarizing question: do M1 and M2 microglia exist? *Nat Neurosci.* 2016;19(8):987-91.

33. De Simone R, et al. Branched-chain amino acids influence the immune properties of microglial cells and their responsiveness to pro-inflammatory signals. *Biochim Biophys Acta.* 2013;1832(5):650-9.

34. Dolci S, et al. Therapeutic induction of energy metabolism reduces neural tissue damage and increases microglia activation in severe spinal cord injury. *Pharmacol Res.* 2022;178:106149.

35. Bonasio R, et al. Molecular signals of epigenetic states. *Science.* 2010;330(6004):612-6.

36. Shafqat A, et al. Cellular senescence in brain aging and cognitive decline. *Front Aging Neurosci.* 2023;15:1281581.

37. Du S, et al. A nerve injury-specific long noncoding RNA promotes neuropathic pain by increasing Ccl2 expression. *J Clin Invest.* 2022;132(13).

38. Chevalier C, et al. Imeglimin: A Clinical Pharmacology Review. *Clin Pharmacokinet.* 2023;62(10):1393-411.

39. Zhang W, et al. High glucose exacerbates neuroinflammation and apoptosis at the intermediate stage after post-traumatic brain injury. *Aging (Albany NY).* 2021;13(12):16088-104.

40. Carpenter KL, et al. Glycolysis and the significance of lactate in traumatic brain injury. *Front Neurosci.* 2015;9:112.

41. Yuan T, et al. Association between blood glucose levels and Glasgow Outcome Score in patients with traumatic brain injury: secondary analysis of a randomized trial. *Trials.* 2022;23(1):38.

42. Liu N, et al. Establishment and Application of a Novel In Vitro Model of Microglial Activation in Traumatic Brain Injury. *J Neurosci.* 2023;43(2):319-32.

43. Sahin M, et al. Transformation of SH-SY5Y cell line into neuron-like cells: Investigation of electrophysiological and biomechanical changes. *Neurosci Lett.* 2021;745:135628.

Figure legends

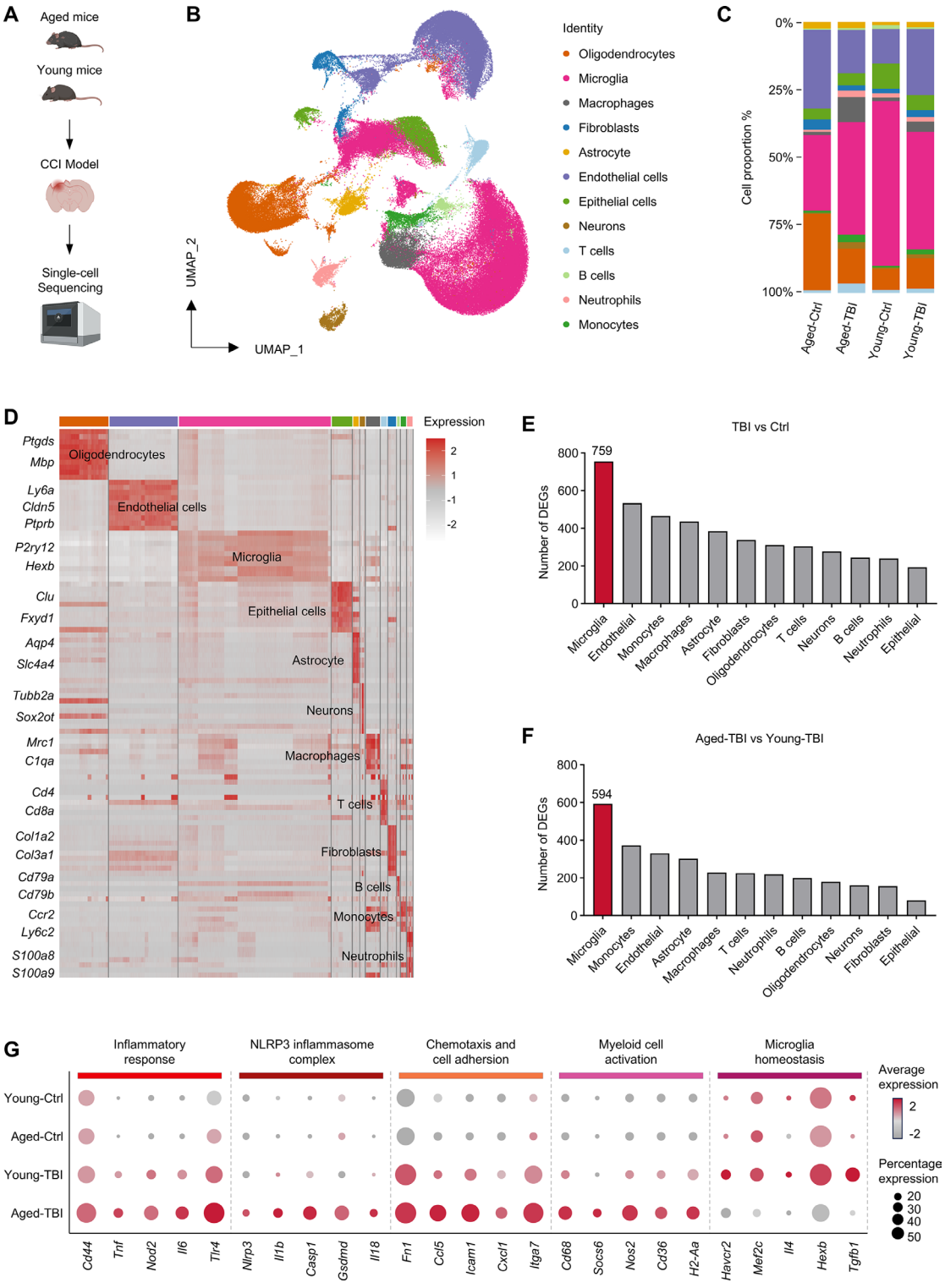

Figure 1. Aging enhances microglia responses after TBI. (A) The injured cerebral hemispheres of aged TBI mice (18-month-old) and young TBI mice (4-month-old) were collected, dissociated, and subjected to single-cell sequencing at day 3 after TBI. n=3/group.

(B) UMAP plot shows different cell types in the brain, distinguished by different colors. **(C)** Proportional stack plots show the percentage of different cell types in the brains from young sham-operated control group (Young-Ctrl), aged sham-operated control group (Aged-Ctrl), young TBI group (Young-TBI), and aged TBI group (Aged-TBI), distinguished by different colors. **(D)** Top10 gene markers for each cell type, characteristic markers are labeled. **(E)** Number of differentially expressed genes (DEGs) between TBI groups and Ctrl groups (adj. $p < 0.05$). Microglia showed the highest number of differentially expressed genes (759 genes). **(F)** Number of differentially expressed genes (DEGs) between Aged-TBI group and Young-TBI group (adj. $p < 0.05$). Microglia showed the highest number of differentially expressed genes (594 genes). **(G)** Expression levels of selected genes in microglia and genes selected from the enriched Gene Ontology (GO) terms in the set of DEGs under different conditions. The size of the dots corresponds to the proportion of cells in each condition and the color indicates the average expression level. The schematic diagram was generated by BioRender.

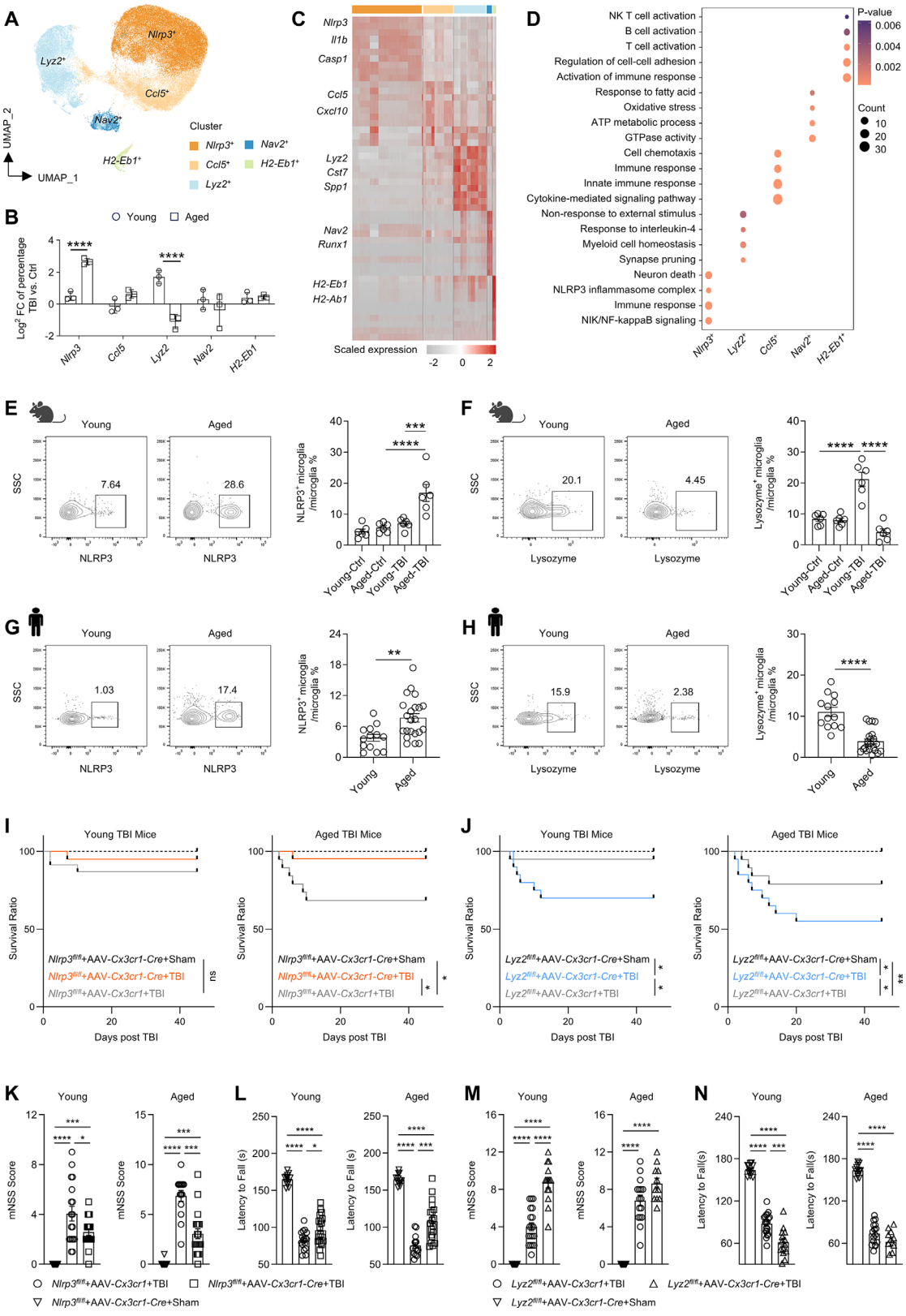

Figure 2. NLRP3$^+$ microglia worsen the prognosis of TBI in the aged. (A) UMAP plot shows the different microglia subpopulations, distinguished by different colors. n=3/group. **(B)** Bar plots show the changes in the proportion of each microglial subset in young and aged mice

before and TBI. n=3/group. **(C)** Gene expression heatmap (top 50 expressed) in microglia subpopulations. **(D)** Functional annotation of different microglia subpopulations. **(E-F)** Representative flowcytometry results and bar plots show the proportions of $NLRP3^+$ and $Lysozyme^+$ microglia in aged and young mice at 3 days before and after TBI. n=6/group. **(G-H)** Representative flow cytometry results show the proportions of $NLRP3^+$ and $Lysozyme^+$ microglia in aged and young TBI patients. Young, n=13; Aged, n=22. **(I)** Survival curves of aged and young mice after AAV-*Cx3cr1-Cre* knockout *Nlrp3* in microglia after TBI (Start: $n_{AAV\text{-}Cx3cr1\text{-}Cre\text{-}Sham}$=12, $n_{AAV\text{-}Cx3cr1\text{-}Cre\text{-}TBI}$=20, $n_{AAV\text{-}Cx3cr1\text{-}TBI}$=20). **(J)** Survival curves of aged and young mice after AAV-*Cx3cr1-Cre* knockout *Lyz2* in microglia after TBI (Start: $n_{AAV\text{-}Cx3cr1\text{-}Cre\text{-}Sham}$=12, $n_{AAV\text{-}Cx3cr1\text{-}Cre\text{-}TBI}$=20, $n_{AAV\text{-}Cx3cr1\text{-}TBI}$=20). **(K)** mNSS scores after 45 days of TBI under different conditions related to (I). Young: $n_{AAV\text{-}Cx3cr1\text{-}Cre\text{-}Sham}$=12, $n_{AAV\text{-}Cx3cr1\text{-}Cre\text{-}TBI}$=19, $n_{AAV\text{-}Cx3cr1\text{-}TBI}$=18. Aged: $n_{AAV\text{-}Cx3cr1\text{-}Cre\text{-}Sham}$=12, $n_{AAV\text{-}Cx3cr1\text{-}Cre\text{-}TBI}$=19, $n_{AAV\text{-}Cx3cr1\text{-}TBI}$=14. **(L)** Rotarod test after 45 days of TBI under different conditions related to (I). The number of animals in each group is consistent with (K). **(M)** mNSS scores after 45 days of TBI under different conditions related to (J). Young: $n_{AAV\text{-}Cx3cr1\text{-}Cre\text{-}Sham}$=12, $n_{AAV\text{-}Cx3cr1\text{-}Cre\text{-}TBI}$=14, $n_{AAV\text{-}Cx3cr1\text{-}TBI}$=19. Aged: $n_{AAV\text{-}Cx3cr1\text{-}Cre\text{-}Sham}$=12, $n_{AAV\text{-}Cx3cr1\text{-}Cre\text{-}TBI}$=11, $n_{AAV\text{-}Cx3cr1\text{-}TBI}$=16. **(N)** Rotarod test after 45 days of TBI under different conditions related to (J). The number of animals in each group is consistent with (M). Data are represented as mean ± SEM. $*P < 0.05$, $**P < 0.01$, $***P < 0.001$, $****P < 0.001$. Statistical analyses were performed using two-tailed unpaired Student's t test (G-H), two-way ANOVA followed by Tukey post hoc test (E-F, K-N) and Kaplan–Meier survival analysis (I-J). The schematic diagram was generated by BioRender.

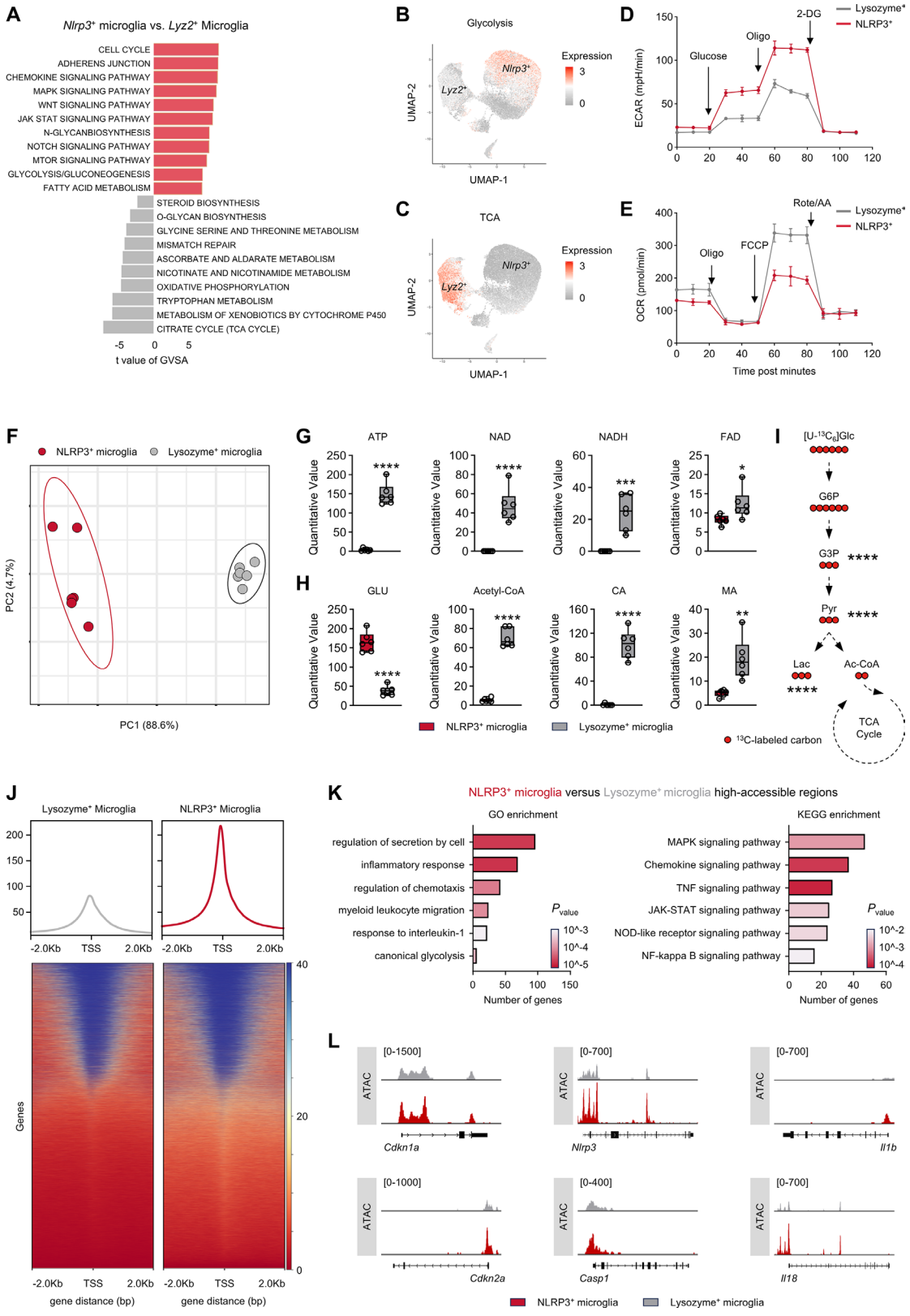

Figure 3. Enhanced aging-induced glycolysis induces the generation of NLRP3$^+$ microglia.

(A) GVSA enrichment of differential biological functions between Nlrp3$^+$ microglia and Lyz2$^+$ microglia. **(B-C)** Gene score feature plots in microglia using representative genes involved in

glycolysis and TCA cycle. **(D)** Line plot shows the results of Extracellular Acidification Rate (ECAR) of NLRP3$^+$ and Lysozyme$^+$ microglia sorted from TBI mice. n=3/group. **(E)** Line plot shows the results of Oxygen Consumption Rate (OCR) of NLRP3$^+$ and Lysozyme$^+$ microglia sorted from TBI mice. n=3/group. **(F)** Distribution of untargeted metabolomics of NLRP3$^+$ microglia and Lysozyme$^+$ microglia in PCA space. n=6/group. **(G-H)** Bar plots show the relative abundance of metabolites related to energy metabolism and TCA cycle in NLRP3$^+$ microglia and Lysozyme$^+$ microglia. n=6/group. **(I)** NLRP3$^+$ microglia from aged TBI mice show significantly higher ^{13}C-labeling efficiency in glyceraldehyde-3-phosphate (G3P), pyruvate, and lactate compared to Lysozyme$^+$ microglia from young TBI mice. n=4/group. **(J)** Density heatmap of differential open chromatin regions in NLRP3$^+$ microglia and Lysozyme$^+$ microglia. n=3/group. **(K)** Gene Ontology (GO) enrichment and Kyoto Encyclopedia of Genes and Genomes (KEGG) enrichment of genes associated with higher chromatin accessibility in NLRP3$^+$ microglia compared to Lysozyme$^+$ microglia. GO: left panel, KEGG: right panel. **(L)** IgV plots show chromatin accessibility of *Cdkn1a* (*p16*), *Cdkm2a* (*p21*), *Nlrp3*, *Casp1*, *Il1b* and *Il18* in NLRP3$^+$ microglia and Lysozyme$^+$ microglia. Data are represented as mean ± SEM. *$P < 0.05$, **$P < 0.01$, ***$P < 0.001$, ****$P < 0.001$. Statistical analyses were performed using two-tailed unpaired Student's t test (G-H).

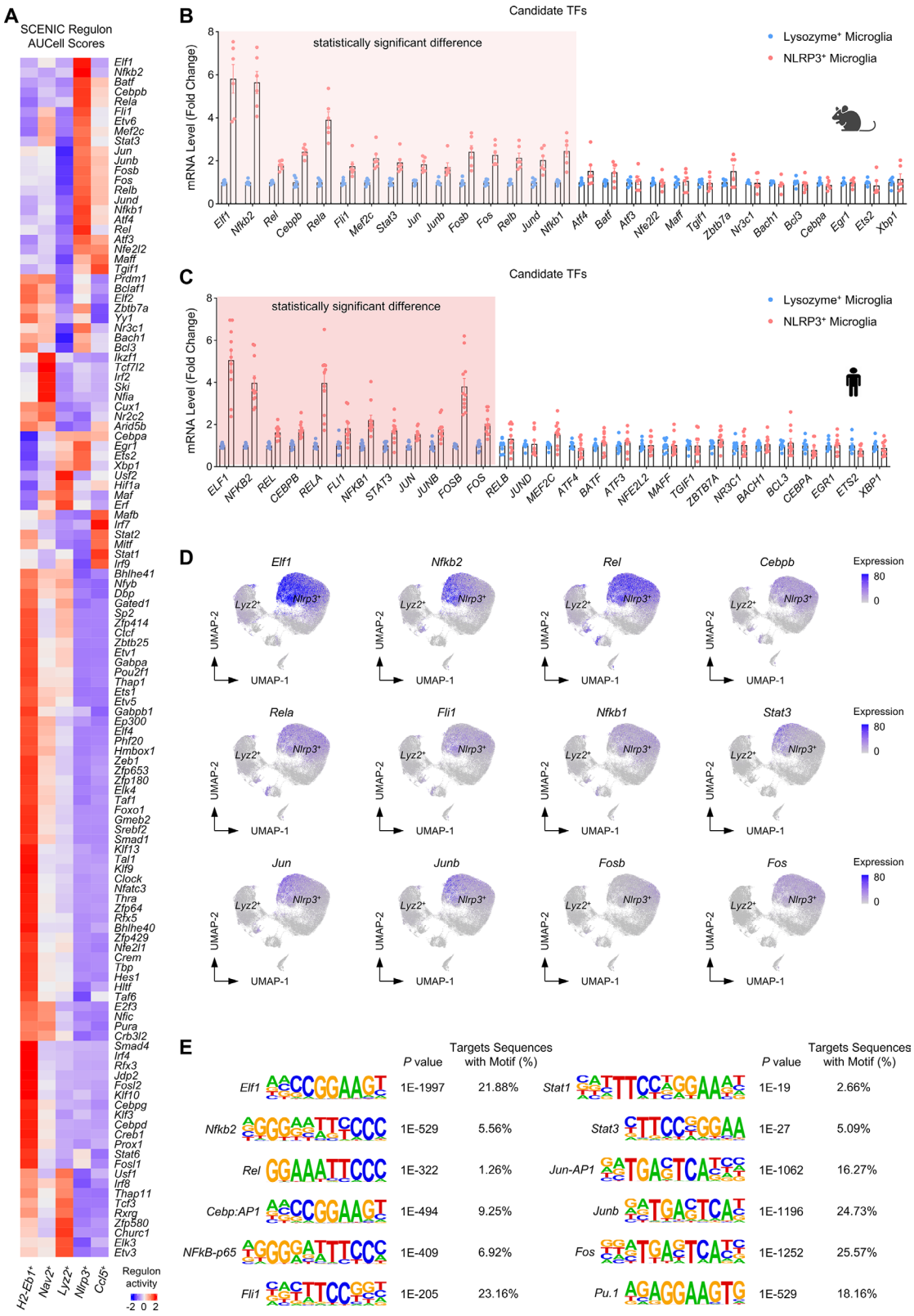

Figure 4. Inflammation-related TFs are associated with the formation of NLRP3$^+$ microglia. (A) SCENIC heatmap of transcription factors (TFs)-regulated microglia subpopulations based on scRNA-seq. **(B)** Bar plots show the qPCR results of 29 alternative TFs

in NLRP3$^+$ microglia and Lysozyme$^+$ microglia sorted from TBI mice. n=6/group. **(C)** qPCR analysis of 29 alternative TFs in NLRP3$^+$ microglia and Lysozyme$^+$ microglia sorted from TBI patients. n_{NLRP3+}=11, $n_{Lysozyme+}$=9. **(D)** Feature plots show the expression of 12 differential TFs co-regulated in human and mouse NLRP3$^+$ microglia in different subpopulations of microglia. **(E)** Tables illustrating the ATAC-seq motif enrichment analysis for NLRP3$^+$ microglia. Data are represented as mean ± SEM. Statistical analyses were performed using two-tailed unpaired Student's t test (B-C). The schematic diagram was generated by BioRender.

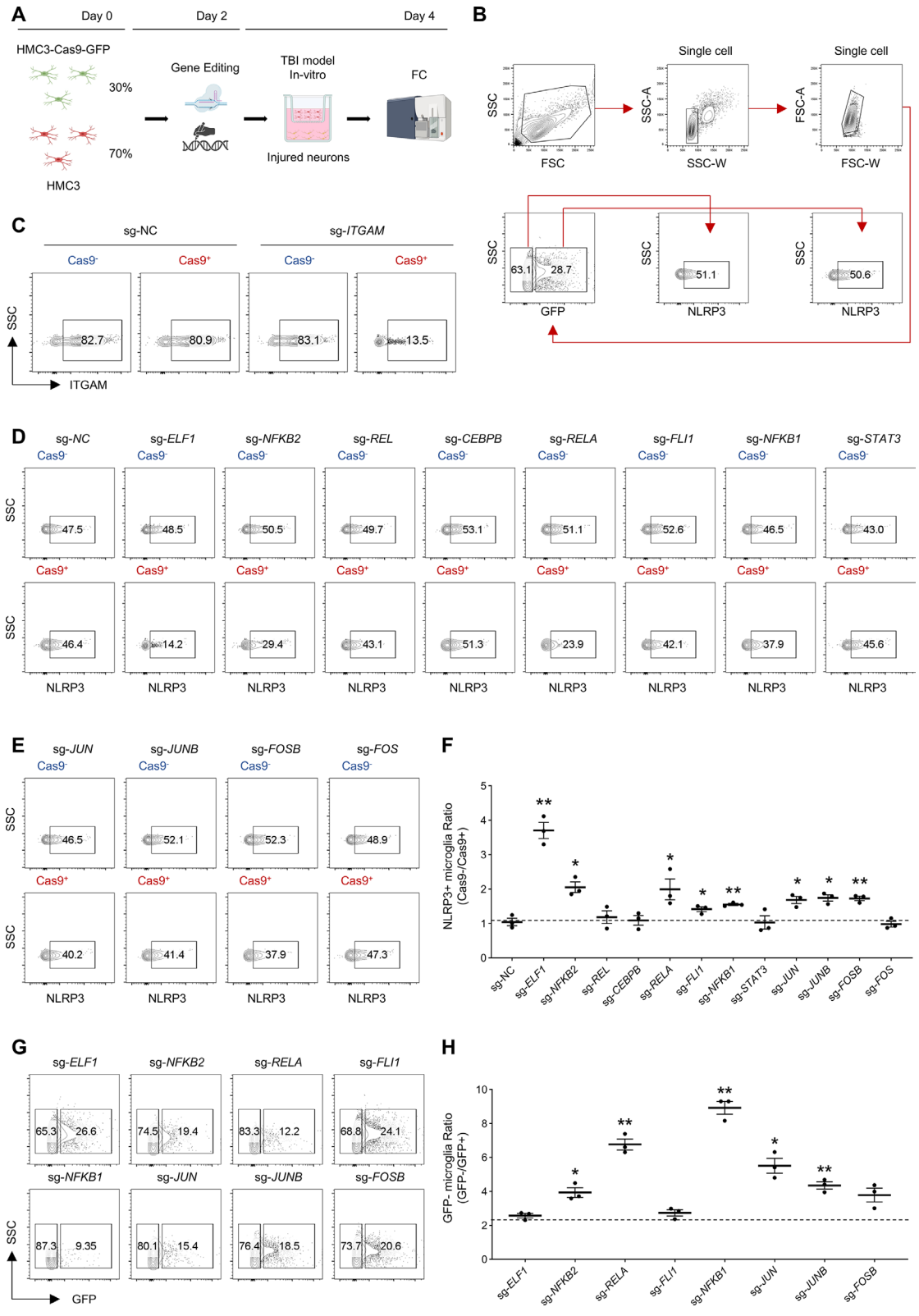

Figure 5. ELF1 predominantly regulates the formation of NLRP3$^+$ microglia. (A) Microglia expressing Cas9-GFP were admixed with normal microglia at a certain ratio, and flow cytometry was performed after two days of co-cultivation with broken neurons using

sgRNA-induced ablation of the target gene. **(B)** Flow cytometry strategy for detecting $NLPR3^+$ microglia in GFP^- ($Cas9^-$) and GFP^+ ($Cas9^+$) microglia. **(C)** Gene editing efficiency of sgRNAs was assayed using sg-*ITGAM*. **(D-F)** Changes in the proportion of $NLRP3^+$ microglia after ablation of 12 alternative transcription factors (TFs). n=3/group. **(G-H)** Changes in the proportion of GFP^-/GFP^+ microglia indicating the cell survival ratio of GFP^+ microglia after ablation of 8 alternative TFs. n=3/group. Data are represented as mean ± SEM. $*P < 0.05$, $**P < 0.01$. Statistical analyses were performed using two-tailed unpaired Student's t test (F, H). The schematic diagram was generated by BioRender.

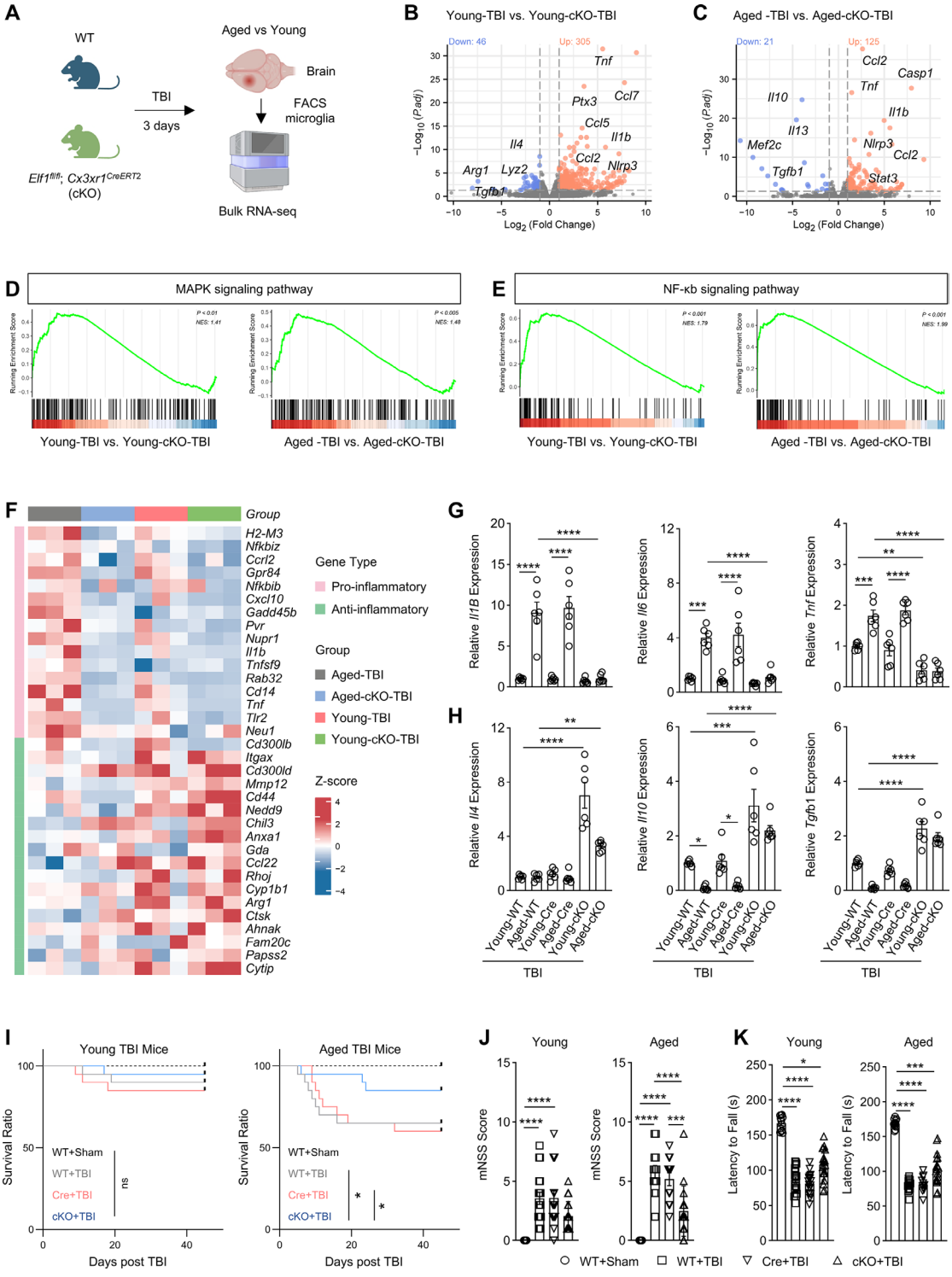

Figure 6. In-vivo ablation of ELF1 improves the survival and neurological recovery of mice after TBI. (A) Brain tissues from WT mice and cKO mice 3 days after TBI were collected, and transcriptome sequencing was performed after FACS enrichment of microglia. **(B)** Volcano plot of microglia DEGs between Young-TBI mice and Young-cKO-TBI mice. n=3/group. **(C)**

Volcano plot of microglia DEGs between Young-TBI mice and Young-cKO-TBI mice. n=3/group. **(D)** GSEA of DEGs in the MAPK signaling pathway between Young-TBI mice and Young-cKO-TBI mice. n=3/group. **(E)** GSEA of DEGs in the NF-κB signaling pathway between Young-TBI mice and Young-cKO-TBI mice. n=3/group. **(F)** Pro-inflammatory and anti-inflammatory expression profiles of different groups of microglia. Each column represents one sample. Data are expressed as z-scores representing the mean and standard deviation normalized expression levels for each gene (row). **(G-H)** qPCR detection of pro- and anti-inflammatory cytokines in different groups of microglia. n=6/group. **(I)** Survival curves of four different conditions mice within 45 days of TBI (Left: Young group, Right: Aged group. Start: $n_{WT+Sham}$=12, $n_{WT+Sham}$=20, $n_{Cre+TBI}$=20, $n_{cKO+TBI}$=20). **(J-K)** mNSS score and Rotarod test of four different conditions mice after 45 days of TBI (Young group, $n_{WT+Sham}$=12, $n_{WT+Sham}$=18, $n_{Cre+TBI}$=17, $n_{cKO+TBI}$=19, Aged group, $n_{WT+Sham}$=12, $n_{WT+Sham}$=13, $n_{Cre+TBI}$=12, $n_{cKO+TBI}$=17). Data are represented as mean ± SEM. *P < 0.05, **P < 0.01, ***P < 0.001, ****P < 0.0001. Statistical analyses were performed using two-way ANOVA followed by Tukey's post hoc test (G-H, J-K) and Kaplan–Meier survival analysis (I). The schematic diagram was generated by BioRender.

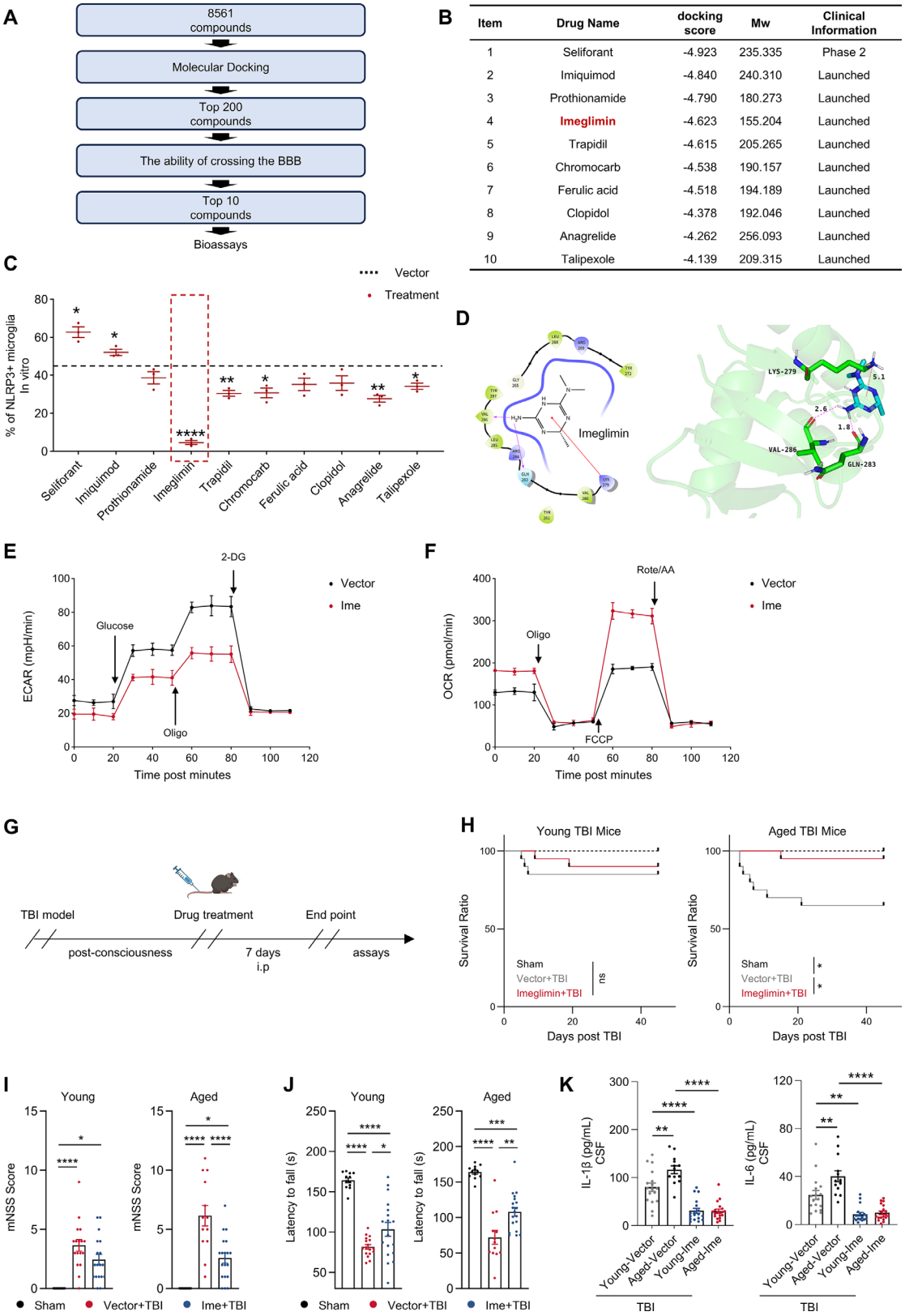

Item	Drug Name	docking score	Mw	Clinical Information
1	Seliforant	-4.923	235.335	Phase 2
2	Imiquimod	-4.840	240.310	Launched
3	Prothionamide	-4.790	180.273	Launched
4	**Imeglimin**	-4.623	155.204	Launched
5	Trapidil	-4.615	205.265	Launched
6	Chromocarb	-4.538	190.157	Launched
7	Ferulic acid	-4.518	194.189	Launched
8	Clopidol	-4.378	192.046	Launched
9	Anagrelide	-4.262	256.093	Launched
10	Talipexole	-4.139	209.315	Launched

Figure 7. Imeglimin treatment promotes recovery in mice with TBI. (A) HTV was performed on 8561 potential ELF1 inhibitor compounds approved by the FDA or already in clinical use. 200 compounds with the highest docking scores were screened after sequential SP

and XP docking analysis. Finally, 10 compounds were screened out of all 200 compounds with the highest potential to cross the blood-brain barrier. **(B)** Docking scores, molecular weights, and clinical information for the 10 compounds selected. **(C)** Ratio of $NLRP3^{+}$ microglia after Imeglimin treatment (HMC3). n=3/group. **(D)** Chemical structure of Imeglimin and in silico docking to the active pocket of the human ELF1 protein. **(E-F)** ECAR and OCR in Imeglimin-treated microglia cell line (HMC3) and vector controls. n=3/group. **(G)** Flow chart of Imeglimin in-vivo treatment of mice with TBI. **(H)** Survival curves of Imeglimin-treated mice versus vector control mice after 45 days of TBI (Left: Young group, Right: Aged group. Start: n_{Sham}=12, $n_{Vector+Sham}$=20, $n_{Ime+TBI}$=20). **(I-J)** mNSS score (M) and rotarod test (N) between Imeglimin-treated mice and vector control mice after 45 days of TBI (Young group, n_{Sham}=12, $n_{Vector+TBI}$=17, $n_{Ime+TBI}$=18, Aged group, n_{Sham}=12, $n_{Vector+TBI}$=13, $n_{Ime+TBI}$=19). **(K)** Concentrations of IL-1β and IL-6 in the cerebrospinal fluid of Imeglimin-treated mice and Vector control mice after 45 days of TBI ($n_{Young\text{-}vector}$=17, $n_{Aged\text{-}vector}$=13, $n_{Young\text{-}Ime}$=18, $n_{Aged+Ime}$=19). Data are represented as mean ± SEM. *$P < 0.05$, **$P < 0.01$, ****$P < 0.0001$. Statistical analyses were performed using two-tailed unpaired Student's t test (C), two-way ANOVA followed by Tukey post hoc test (I-K) and Kaplan–Meier survival analysis (H). The schematic diagram was generated by BioRender.